DOT/FAA/TC-17/48

Preliminary Testing of Low Reynolds Number Aerodynamics for a Swept Wing With Artificial Ice Roughness

September 2017

Final Report

This document is available to the U.S. public through the National Technical Information Services (NTIS), Springfield, Virginia 22161.

This document is also available from the Federal Aviation Administration William J. Hughes Technical Center at actlibrary.tc.faa.gov.

U.S. Department of Transportation
Federal Aviation Administration

NOTICE

This document is disseminated under the sponsorship of the U.S. Department of Transportation in the interest of information exchange. The U.S. Government assumes no liability for the contents or use thereof. The U.S. Government does not endorse products or manufacturers. Trade or manufacturers' names appear herein solely because they are considered essential to the objective of this report. The findings and conclusions in this report are those of the author(s) and do not necessarily represent the views of the funding agency. This document does not constitute FAA policy. Consult the FAA sponsoring organization listed on the Technical Documentation page as to its use.

This report is available at the Federal Aviation Administration William J. Hughes Technical Center's Full-Text Technical Reports page: actlibrary.tc.faa.gov in Adobe Acrobat portable document format (PDF).

Technical Report Documentation Page

1. Report No. DOT/FAA/TC-17/48	2. Government Accession No.	3. Recipient's Catalog No.
4. Title and Subtitle PRELIMINARY TESTING OF LOW REYNOLDS NUMBER AERODYNAMICS FOR A SWEPT WING WITH ARTIFICIAL ICE ROUGHNESS		5. Report Date September 2017
		6. Performing Organization Code
7. Author(s) Brian S. Woodard, Andy P. Broeren, Jeffrey M Diebold, and Michael B. Bragg		8. Performing Organization Report No.
9. Performing Organization Name and Address University of Illinois at Urbana-Champaign University of Washington 306 Talbot Laboratory, MC-236 Aeronautics & Astronautics 104 South Wright Street Box 352400 Urbana, Illinois 61801 Seattle, WA 98195-2400 NASA Glenn Research Center Icing Branch MS 11-2 21000 Brookpark Rd. Cleveland, OH 44135		10. Work Unit No. (TRAIS)
		11. Contract or Grant No.
12. Sponsoring Agency Name and Address FAA Northwest Mountain Regional Office 1601 Lind Ave SW Renton, WA 98057		13. Type of Report and Period Covered Final Report
		14. Sponsoring Agency Code ANM-112

15. Supplementary Notes

The FAA William J. Hughes Technical Center Aviation Research Division COR was Jim Riley.

16. Abstract

This report presents key results of preliminary testing of iced swept-wing aerodynamics at low Reynolds numbers. This investigation is part of a larger collaborative research effort on ice accretion and aerodynamics for swept wings. The testing was conducted in the 7 x 10 ft wind tunnel facility at Wichita State University using a Common Research Model-based semispan model. The model was constructed with a removable leading edge (RLE) so that artificial ice shapes could be readily attached. Rapid prototyping manufacturing was used to simulate full-span ice roughness with hemispherical elements of approximately 0.01 in. The traditional method of ice roughness simulation—addition of grit roughness to the clean wing—was also performed for comparison. A RLE of a horn ice shape, determined using computational fluid dynamics, was also tested. Several splitter plate configurations for isolating the wing from the wind tunnel's floor boundary layer were tested, and a circular splitter plate and streamlined shroud were selected as the baseline configuration for this and future tests. The effects of Reynolds number and Mach number on the clean wing were investigated, but only limited conclusions could be drawn without further testing in a facility where Reynolds number and Mach number can be controlled independently. The Reynolds number and Mach number effects were small compared to the overall aerodynamic effect of the ice versus the clean-wing performance. Results from the iced wing configurations showed that defining an unambiguous stalling angle was difficult using only performance-based parameters, and general criteria need to be developed for future testing. The aerodynamic performance differences between the various roughness sizes and applications types were small, especially at low angles of attack. However, spanwise roughness variations produced relatively significant aerodynamic differences between cases, indicating that artificial ice shapes must be carefully designed to avoid inadvertently affecting the flowfield. The surface oil flow visualization results supported that conclusion by highlighting the aerodynamic effects of the spanwise discontinuities.

17. Key Words Swept wing icing, Inflight icing, Icing wind tunnel, Swept wing ice shapes, Swept wing model	18. Distribution Statement This document is available to the U.S. public through the National Technical Information Service (NTIS), Springfield, Virginia 22161. This document is also available from the Federal Aviation Administration William J. Hughes Technical Center at actlibrary.tc.faa.gov.		
19. Security Classif. (of this report) Unclassified	20. Security Classif. (of this page) Unclassified	21. No. of Pages 62	22. Price

Form DOT F 1700.7 (8-72)   Reproduction of completed page authorized

TABLE OF CONTENTS

LIST OF FIGURES

LIST OF TABLES

LIST OF ACRONYMS

α	Angle of attack
b	Semispan
c	Chord length
C_D	Wing total drag coefficient
C_L	Wing lift coefficient
C_M	Wing pitching moment coefficient
c_{mac}	Chord length of mean aerodynamic chord
C_p	Pressure coefficient
D	Drag Force
F_A	Axial Force
F_N	Normal Force
k	Roughness element height
L	Lift Force
M	Mach number, Pitching moment
M_{bal}	Pitching moment measured at force balance reference point
q_∞	Free-stream dynamic pressure
R	Resultant quantity in uncertainty analysis
Re	Reynolds number
S	Wing planform reference area
U_α	Uncertainty in angle of attack
U_{CL}	Uncertainty in lift coefficient
U_{cmac}	Uncertainty in wing mean aerodynamic chord length
U_D	Uncertainty in drag force
U_{FA}	Uncertainty in axial force
U_{FN}	Uncertainty in normal force
U_L	Uncertainty in lift force
U_M	Uncertainty in pitching moment measured at model reference point
U_{Mbal}	Uncertainty in pitching moment measured at force balance reference point
$U_{q\infty}$	Uncertainty in free-stream dynamic pressure
U_R	Uncertainty in resultant quantity
U_S	Uncertainty in wing planform reference area
U_{xi}	Uncertainty in generic variable
U_{xoff}	Uncertainty in offset distance between force balance reference point and model reference point
x	Chordwise coordinate
x_i	Generic variable in uncertainty analysis
x_{off}	Distance along the x-axis of the force balance between the balance reference point and the model reference point
y	Spanwise coordinate
z	Vertical coordinate
y/b	Nondimensional spanwise location
CAD	Computer-aided design
CFD	Computational Fluid Dynamics
CRM	Common Research Model

ESP	Electronic pressure scanning
IRT	Icing Research Tunnel
MAC	Mean Aerodynamic Chord
ONERA	Office National d´ Etudes et de Recherches Aérospatiales
RLE	Removable leading edge
RPM	Rapid prototype manufacturing
SLA	Stereolithography
WSU	Wichita State University

EXECUTIVE SUMMARY

This report presents key results of preliminary testing of iced swept-wing aerodynamics at low Reynolds numbers. This investigation is part of a larger collaborative research effort on ice accretion and aerodynamics for swept wings. Ice accretion and the resulting aerodynamic effects on large-scale swept wings presents a significant airplane design and certification challenge for airframe manufacturers, certification authorities, and research organizations. Though the aerodynamic effects of ice accretion on straight wings has been extensively studied and is well understood, the available data on swept-wing icing is extremely sparse.

The testing was conducted in the 7 x 10 ft wind tunnel facility at Wichita State University using a Common Research Model-based semispan model. The model was constructed with a removable leading edge (RLE) so that artificial ice shapes could be readily attached. Rapid prototyping manufacturing (RPM) was shown to be capable of producing roughness elements of approximately 0.01 in., and full-span roughness ice shapes were created using RPM. The traditional method of ice roughness simulation—addition of grit roughness to the clean wing—was also performed for comparison to RPM. A RLE of a horn ice shape, determined using computational fluid dynamics, was also tested. Several splitter plate configurations for isolating the wing from the wind tunnel's floor boundary layer were manufactured and tested. Based on the aerodynamic performance results, a circular splitter plate and streamlined shroud were selected as the baseline configuration for this and future tests.

The effects of Reynolds number and Mach number on the clean wing were investigated, but only limited conclusions could be drawn without further testing in a facility where Reynolds number and Mach number can be controlled independently. For the leading edge configurations with roughness and horn ice, the Reynolds number and Mach number effects were small compared with the overall effect of the ice compared to the clean-wing performance. Results from the iced-wing configurations showed that defining an unambiguous stalling angle was difficult using only performance-based parameters, and general criteria need to be developed for future testing. The performance differences between the various roughness sizes and applications types (rapid prototype manufactured or grit applied to the clean model) were small, especially at low angles of attack. However, spanwise roughness variations produced relatively significant aerodynamic differences between cases, indicating that the artificial ice shapes must be carefully designed to avoid inadvertently affecting the flowfield. The surface oil flow visualization results supported that conclusion by highlighting the aerodynamic effects of the spanwise discontinuities for the roughness and horn-ice-shape configurations. These tests provided a useful preliminary study to guide future low and high Reynolds number swept-wing icing testing.

1. INTRODUCTION

This report presents the key results of a preliminary assessment of iced swept-wing aerodynamics at low Reynolds number. This investigation was undertaken as a part of a larger collaborative research effort on ice accretion and aerodynamics for large-scale swept wings. Section 1.1 provides a description of this larger effort and the role of the present investigation within it. The specific objectives and approach for this work are addressed in section 1.2.

1.1 BACKGROUND

Ice accretion and the resulting aerodynamic effect on large-scale swept wings presents a significant airplane design and certification challenge to airframe manufacturers, certification authorities, and research organizations. Broeren et al. [1] described a large, collaborative research project of FAA, NASA, and Office National d´ Etudes et de Recherches Aérospatiales (ONERA) addressing this challenge. The report stated:

> Computational fluid dynamics codes have reached a level of maturity that they are being proposed by manufacturers for use in certification of aircraft for flight in icing. However, sufficient high-quality data to evaluate their performance on iced swept wings are not currently available in the public domain [1].

FAA, NASA, and ONERA developed a seven-phase effort to advance the state-of-the-art large-scale swept wing ice accretion simulation and aerodynamics. Research already completed includes:

1. Development of a swept-wing aerodynamics-based ice accretion classification system [2, 3].
2. Development of 3-D aerodynamic measurement methods specifically for iced swept wings [4–6].
3. Development and validation of 3-D measurement methods to quantify ice accretion geometry in the NASA Icing Research Tunnel (IRT) [7–11].
4. Development of hybrid model design methods for testing large-scale swept-wing sections in the NASA IRT [12–17].
5. Generation of a set of 3-D ice accretion geometries on three different sections of a full-scale swept wing through three IRT test campaigns.
6. Preliminary computational fluid dynamics (CFD) analysis of hybrid model geometries in the IRT and assessment of aerodynamic effects [18–21].

Research planned for completion of the effort includes:

- Development, design, and fabrication of both high- and low-fidelity artificial ice shapes based on the ice accretion database generated from the IRT tests.
- Low and high Reynolds number aerodynamic testing of a swept-wing model with artificial ice shapes.
- Continued development and assessment of computational tools for ice accretion and aerodynamics simulation.

1

- Determination of the ice-shape geometric fidelity required for accurate iced-wing aerodynamics.

A detailed discussion of this effort is beyond the scope of this report, and the reader is referred to references cited in the following paragraph for more information.

In past studies of icing effects on airfoil performance, systematic investigations of Reynolds and Mach number effects were conducted [22–28]. Over the course of many years, it was found that aerodynamic tests conducted in the Reynolds number range of 1.0 to 2.0×10^6 could yield results applicable to flight Reynolds number (e.g., 10 to 20×10^6) for leading-edge ice shapes. Therefore, a significant effort has been planned to determine if similar trends apply for full-span, leading-edge ice on a swept wing. This effort involves both low and high Reynolds number aerodynamic testing. Low Reynolds number aerodynamic testing will be conducted in the Wichita State University (WSU) 7 x 10 ft atmospheric wind tunnel, described in section 2.1. The high Reynolds number aerodynamic testing will be conducted in the ONERA F1 11.4 x 14.8 ft pressurized wind tunnel. The pressurization capability of this facility will allow for independent variation of Reynolds number up to approximately 10×10^6 and Mach number up to approximately 0.36. Because of the differences in the test section sizes, the ONERA F1 semispan wind tunnel model will be 1.5 times larger than the model tested in the WSU facility. The results from the ONERA F1 test campaigns will be analyzed for Reynolds and Mach numbers and other effects and will be compared with the results of the WSU test campaigns to determine the extent to which iced, swept-wing aerodynamic testing can be conducted in smaller-scale facilities at lower Reynolds number.

Broeren et al. [1] described the swept-wing model selected for this research. It is explained that, for this research to be relevant and useful, it is important that the wing geometry be representative of current, modern commercial aircraft designs. In addition, the geometry must be publicly available with no distribution restrictions. Based on these criteria, the Common Research Model (CRM) was selected. The modern, supercritical wing design was developed with NASA support for another research effort [29] and is well suited for this work. The CRM wing was designed for a wide-body commercial transport airplane similar in size to a Boeing 777. This very large geometry presented some significant scaling challenges for this work. Given the magnitude of the technical tasks already being undertaken in this effort, a 65% scale version of the CRM wing was selected as the full-scale reference geometry. Even with this scale reduction, the CRM65 wing is still representative of the size of a Boeing 757. The CRM65 semispan wing and its dimensions are shown in figure 1. The portion of this geometry used for the low and high Reynolds number aerodynamic tests was the entire wing semispan from the fuselage side-of-body plane at 10% semispan to the wing tip. A scale reduction to 8.9% in model size was required for the low Reynolds number aerodynamic testing. Given this significant scale reduction and increased complexity associated with semispan model testing, a number of technical tasks were identified and investigated as described in this preliminary report.

65% Scale CRM Characteristics
- Semispan = 62.7 ft
- Root chord (symmetry plane) = 29.0 ft
- Root chord (fuselage side of body) = 25.4 ft
- Tip chord = 5.8 ft
- Mean aerodynamic chord = 15.0 ft
- Semispan area = 873 ft^2
- Aspect Ratio = 9.0
- Taper Ratio = 0.28
- Sweep angle (c/4) = 35 deg.

Yehudi break, 37% semispan

Fuselage side of body,10% semispan

Symmetry plane
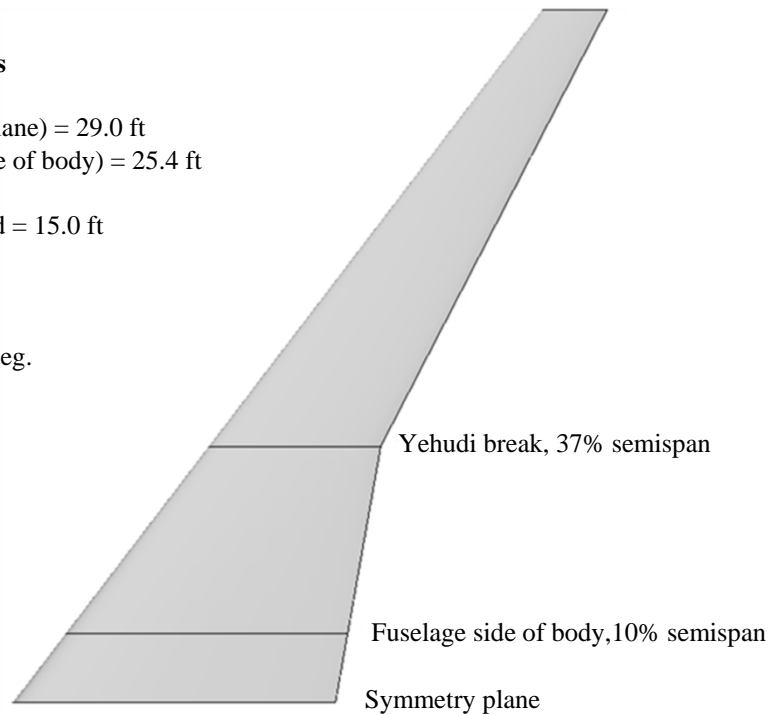
Figure 1. Summary of 65% scale CRM geometric characteristics from Broeren et al. [1]

One such technical task was determining an appropriate way to install the semispan swept wing model in a wind-tunnel test section. Unlike the case for 2-D airfoil testing, there is much less guidance on best practices in the technical literature. Diebold et al. [30, 31] described the various possible configurations and their respective advantages and disadvantages. They cited some limited examples of previous work that are available. A significant consideration is the interaction of the wind-tunnel test section floor boundary layer with the swept-wing flowfield. There are several methods that have been used to minimize this interaction and any resulting adverse effect on the wing performance (e.g., floor boundary-layer control such as suction, wing installation with some type of fuselage pod and standoff, or wing installation with a splitter plate). For this research, the splitter-plate installation approach was selected because of its simplicity and associated lower costs of manufacturing. However, it was found that there is little design guidance on splitter plates in the literature. Diebold et al. [30] summarized the results of an investigation into important parameters and effects for semispan wing splitter plates. Because their investigation was conducted at very small scale at very low Reynolds number, further exploration was required. This resulted in several candidate configurations for use in the swept-wing icing research effort. These configurations were evaluated in this study.

Another technical task critical to the success of both low and high Reynolds number aerodynamic test campaigns is the design and fabrication of high-fidelity artificial ice shapes that can be attached to the leading edge of the swept-wing model. This task is complicated by several factors including the small scale of the wind-tunnel model along with the large variation in the wing geometry across the span of the model (i.e., twist and taper). In past aerodynamic studies of iced airfoils using the mold-and-casting method to develop the artificial ice shape (see [23–25], [27–28]), the scale of the aerodynamic model was identical to that for which the ice accretion was generated. Because

3

those models were 2-D, there was no geometric scale variation along the span. Therefore, for this research project, methods were developed and validated for creating scaled, high-fidelity artificial ice shapes with significant scale variation in the spanwise direction.

This problem provided the motivation for the development and validation of 3-D measurement methods for ice accretion in the NASA IRT [1]. Having fully 3-D measurements of the ice accretion in digital form makes it possible to scale the iced geometry for smaller wind-tunnel model size and make spanwise changes in the ice geometry. Note that the ice accretions were generated in the IRT on full-scale sections of the CRM65 leading edge, therefore requiring considerable scale reduction for aerodynamic testing. Once the ice accretion geometry is defined from the IRT data, it must be mated to the aerodynamic wind-tunnel model geometry and then fabricated such that it can be attached to the leading edge in a robust, accurate, and precise manner. Rapid prototype manufacturing (RPM) methods such as stereolithography (SLA) have been used successfully in past icing aerodynamics research (see [10, 23, 25, 32]). However, the model scale factors and spanwise wing geometry variations were considered extreme enough in this work to warrant further exploration.

The effect of the large reduction to 8.9% scale on roughness and feather features in the IRT ice accretions was of particular concern because of their potential aerodynamic importance. The full-scale size of these features in the IRT could be 0.1 in. or smaller. This translates to a size of 0.01 in. or smaller on the 8.9% scale wing. Features of this size approach the lower size limit for some types of RPM methods. Therefore, assessment of the ability to produce such features was required.

The technical concerns cited above provided motivation for conducting a preliminary low Reynolds number aerodynamic test campaign with the 8.9% scale CRM65 semispan wind-tunnel model. The investigation focused on mitigating the risk of unknown problems affecting the planned testing of high-fidelity artificial ice shapes at both low and high Reynolds numbers. Therefore, this report does not provide an extensive technical analysis of the clean- and iced-wing performance because future test campaigns are planned with this specific objective. This report instead presents key results and provides guidance for the successful completion of the planned test campaigns.

1.2 OBJECTIVES AND APPROACH

The overall goal of this preliminary investigation was to determine methods to minimize technical risks associated with low and high Reynolds number aerodynamic testing of a swept wing with high-fidelity artificial ice shapes. This work had the following specific objectives:

- Evaluate splitter plate configurations suitable for both the 8.9% scale, low Reynolds number, and the 13.3% scale high Reynolds number aerodynamic wind-tunnel models.
- Evaluate the ability of RPM methods to capture small-size roughness features associated with ice accretion.
- Evaluate the ability of RPM methods to fabricate artificial ice shapes with sufficient accuracy to be instrumented and attached accurately and precisely to the leading edge of the 8.9% scale wing.

- Generate a preliminary assessment of low Reynolds number swept-wing performance in the clean configuration for baseline data and with artificial ice roughness to investigate aerodynamic sensitivity.

To meet these objectives, aerodynamic testing was conducted at the WSU 7 x 10 ft wind tunnel using the 8.9% scale semispan wing model of the CRM65. Different wing mounting configurations were tested with and without various splitter plate combinations. The aerodynamic results were analyzed, and a final mounting configuration was selected for the remainder of the test campaign. Artificial ice roughness was developed using regular patterns of hemispherical geometry. This was incorporated into the removable portion of the wing leading-edge model, fabricated using SLA. The resulting artificial ice shapes were also instrumented to measure surface static pressure. For comparison purposes, an artificial ice shape of a large, glaze-horn geometry was also designed, fabricated with SLA, and instrumented. Silicon-carbide grains were also used to simulate small ice roughness. Grit sizes similar to the hemispherical roughness sizes were applied to the wing leading edge. Aerodynamic performance testing was conducted in angle of attack sweeps over a Reynolds number range of 0.8×10^6 to 2.4×10^6 and a corresponding Mach number range of 0.09–0.27. Force balance and surface pressure data were acquired. Surface-oil flow visualization was also performed for a subset of the configurations. Details regarding the experimental setup, model design, and artificial ice shapes are provided in section 2. The results of this work are presented and discussed in section 3. Finally, section 4 contains a summary and conclusions of this preliminary investigation and recommendations for the planned test campaigns.

2. EXPERIMENTAL METHODS AND APPARATUS

2.1 WIND-TUNNEL FACILITY

2.1.1 Wichita State University 7 x 10 ft Wind Tunnel

All experiments discussed in this report were carried out in the Walter H. Beech Wind Tunnel at WSU. The tunnel is an atmospheric, return-type, subsonic wind tunnel with a 7 x 10 ft test section. The maximum speed of the tunnel is approximately 350 ft/s, which corresponds to a Reynolds number per foot of approximately 1.8×10^6/ft and a maximum dynamic pressure of 125 psf. The dynamic pressure can be held to within ±0.1 psf over the entire operating range. The freestream turbulence intensity in the central region of the test section is approximately 0.07% of the freestream velocity.

Load measurements were performed using a six-component pyramidal-style force balance located beneath the test-section floor [33]. This study used a reflection plane model, and the force balance was used to measure the lift, drag, and pitching moment. The force balance does not directly measure the lift and drag, but rather measures the normal force (F_N) and the axial force (F_A), which are relative to a coordinate system fixed to the force balance. A coordinate rotation is required to determine the lift and drag in the wind axes. These relationships are given in equations 1 and 2.

$$L = F_N \cos(\alpha) - F_A \sin(\alpha) \tag{1}$$

$$D = F_A \cos(\alpha) + F_N \sin(\alpha) \tag{2}$$

The force balance measures the moment about a reference point fixed to the force balance, and it is necessary to transfer the moment to the reference point on the model. For the model used in this study, there was an offset along the x-axis of the force balance between the balance reference point and the model reference point. This offset, defined as x_{off}, was 4.5 inch. There was no offset along the z-axis. The pitching moment measured by the balance is denoted by M_{bal} and moment about the model reference point is denoted by M. The relationship between the two moments is given in equation 3:

$$M = M_{bal} + F_N x_{off} \qquad (3)$$

The accuracy of the balance was 0.02% of full scale. The full range and the full-scale accuracy of these measurements are listed in table 1. The uncertainty in the measured dynamic pressure was approximately 0.1 psf. The uncertainties in the relevant aerodynamic coefficients are discussed below.

Table 1. Full-scale range and accuracy of the WSU Wind Tunnel

Measurement	Range	Full-Scale Accuracy
F_N (lbf)	±1984	±0.794
F_A (lbf)	±794	±0.317
M_{bal} (lbf-ft)	±839	±0.336

Surface pressure measurements were acquired using miniature electronic pressure scanning (ESP) modules developed by Esterline (model ESP-32HD). An ESP module with a range of ±10.0 psid was used for pressure taps located near the leading edge of the model. For the remaining pressure taps, a module with a range of ±2.0 psid was used. The accuracy, in percent of full-scale, was ±0.03% and ±0.06% for the 10 psid and the 2 psid module, respectively. This corresponds to an uncertainty of 0.003 psid and 0.0012 psid for the two modules.

2.1.2 Wind-Tunnel Wall Corrections

All aerodynamic data (i.e., α, C_L, C_M, C_D, and C_p) presented in this report were corrected for wind tunnel wall effects using the standard procedure for 3-D models outlined in Pope et al.[33] as implemented by WSU [34]. It should be noted that these corrected results are considered preliminary. The standard wind-tunnel wall corrections for swept-wing, reflection-plane models involve numerous assumptions that require further evaluation as to their suitability for the performance data to be acquired in the planned test campaigns, particularly with respect to the wing with leading-edge ice shapes.

As described in section 1.1, aerodynamic data acquired at the WSU wind tunnel will be compared with data acquired at the ONERA F1 facility. Therefore, it is important that the effect of the wind-tunnel walls on the aerodynamic data from both facilities be accounted for properly. In addition, CFD simulations will also be performed and compared to the experimental results. Wall corrections on the experimental data will also be important for comparison to CFD simulation results that do not model the presence of the wind-tunnel walls. The remainder of this section

provides a description of the primary wind-tunnel-wall effects and the potential limitations of the correction procedure used for the preliminary data in this report.

The walls of a wind tunnel alter the boundary conditions of the flow, and this added restriction influences the freestream conditions seen by the model. The magnitude of the wall effects depends on the geometry of the model and the wind-tunnel test section. Therefore, it cannot be assumed that measurements acquired in different facilities should necessarily match until these effects have been properly considered. The most important wind-tunnel-wall effects are buoyancy, solid blockage, wake blockage, and streamline curvature [33].

The buoyancy correction accounts for a streamwise gradient in the static pressure due primarily to the growth of the boundary layers along the tunnel walls. The growing boundary layers effectively reduce the cross-sectional area of the test section causing the flow to accelerate and the freestream static pressure to decrease, resulting in an increase in the drag of the model. In the WSU 7 x 10 ft wind tunnel, the magnitude of this streamwise pressure gradient is known [34], and Pope et al. [33] discussed how to correct the drag for the buoyancy effect.

In a closed test section, the maximum cross-sectional area is fixed by the walls, and when a model is placed within the test section, the effective cross-sectional area seen by the flow is reduced. Because of conservation of mass, the flow must accelerate, and the model experiences a higher freestream dynamic pressure. This effect is referred to as solid blockage. A similar effect, referred to as wake blockage, is caused by the wake of the model. To compensate for the low-speed flow in the wake, the freestream must accelerate. The solid blockage is generally considered to be a function of only the geometry of the model and test section. Wake blockage depends on the size of the wake and therefore is a function of geometry and the drag on the model. Blockage corrections are typically only applied to the freestream velocity and dynamic pressure.

A lifting body induces curvature throughout the flowfield. In a wind tunnel, this curvature is constrained by the solid walls altering the flow around the model. Corrections for streamline curvature effects are typically applied to the angle of attack, the pitching moment, and the induced drag [33].

Nearly all standard wall corrections require the use of correction factors that are typically read from charts. Many of these charts can be found in Pope et al. [33]. The values in the charts were usually determined by representing the wind tunnel and model with distributions of sources, sinks, and vortices. In addition, the values in the charts are usually only for specific geometries that may not be representative of the current model. As a result, engineering judgment is often required to determine the appropriate value read on the chart. In the case of 3-D models, the streamwise curvature corrections were developed, assuming either uniform or elliptical spanwise lift distributions. This assumption may not be valid for a swept wing, especially with a complex leading-edge ice accretion, and should be evaluated.

For the experiments discussed in this report, the presence of the splitter plate may add complications. Correction factors for the solid blockage effect of fuselages have been calculated, but no similar calculations for splitter plates exist. In addition, the blockage induced by the splitter plate will result in an accelerated flow that will be felt primarily over the inboard sections of the model, whereas standard blockage corrections assume a constant change in the dynamic pressure

along the span of the wing. The wake blockage factor depends on the measured drag of the model. For this test, the splitter plate is not connected to the force balance, so its drag is not measured. Therefore, the standard wake blockage procedure does not account for the wake of the splitter plate and should be evaluated.

This discussion has outlined the standard wind-tunnel-wall correction procedures implemented in this preliminary investigation. The discussion has also indicated potential shortcomings of these methods that should be addressed in future test campaigns. The overall research effort involves comparisons of data among different wind-tunnel facilities and CFD simulations, so these corrections must be well understood and properly applied. Determining the adequacy of these wall correction procedures will require additional research into these methods and may require CFD simulations performed with and without tunnel wall to more closely investigate these effects.

2.1.3 Experimental Procedure

The experiments performed during this campaign included force balance measurements and surface oil flow visualization. The model angle of attack was varied from -6° to 16°. Measurements were acquired at Reynolds numbers of 0.8×10^6, 1.6×10^6, and 2.4×10^6, which corresponded to freestream Mach numbers of 0.09, 0.18, and 0.27, respectively. During the run, the dynamic pressure was held to within ±0.1 psf. The general procedure was as follows:

1.   Set desired speed.
2.   Measure tunnel conditions.
3.   Acquire force balance and surface pressure measurements.
4.   Set new angle of attack and repeat steps 1–3.

Surface oil flow visualization was performed by applying a mixture of mineral oil and fluorescent dye to the surface of the wing. The shear forces from the wind move the oil along the surface creating a time-averaged pattern of the flow near the surface. This technique can be used to detect features such as separated flow, vortices, and laminar to turbulent transition. The surface was covered with black contact paper prior to applying the oil to the model. The black surface of the contact provided high contrast between the model surface and the fluorescent oil. The general process is described below:

1.   Apply a coat of 10W-30 motor oil to the surface of the contact paper. This thin layer of oil allows the fluorescent dye mixture to flow more easily.
2.   Apply the mixture of mineral oil and fluorescent dye to the surface using a paint roller.
3.   Set the desired angle of attack.
4.   Set the desired freestream velocity.
5.   Allow the tunnel to run for 1–2 minutes.
6.   Shut off the tunnel, and set the angle of attack to 0°.
7.   Place UV lamps within the test section so that the oil fluoresces.
8.   Acquire images using a standard DSLR camera. The exposure The exposure time and aperture stop (f-number) are dependent on the amount of oil on the surface and how well the UV lamps illuminate the model surface.
9.   Repeat steps 2–8 for a new angle of attack or speed (it was occasionally necessary to reapply the motor oil).

2.1.4 Uncertainty Analysis

The uncertainty in the relevant aerodynamic coefficients can be determined using the standard method outlined by Coleman and Steel [35]. This method assumes that a derived result, R, is a function of n variables x_i, $i = 1, \dots, n$.

$$R = R(x_1, x_2, x_3, \dots, x_n) \tag{4}$$

The uncertainty in R is denoted as U_R and is calculated using the following equation, where U_{xi} is the uncertainty in x_i:

$$U_R = \sqrt{\sum_{i=1}^{n} \left(\frac{\partial R}{\partial x_i} U_{x_i}\right)^2} \tag{5}$$

As an example, the lift coefficient is defined as:

$$C_L = \frac{L}{q_\infty S} \tag{6}$$

Using equation 6, the uncertainty in the lift coefficient can be expressed as:

$$U_{C_L} = \sqrt{\left(\frac{\partial C_L}{\partial L} U_L\right)^2 + \left(\frac{\partial C_L}{\partial q_\infty} U_{q_\infty}\right)^2 + \left(\frac{\partial C_L}{\partial S} U_S\right)^2} \tag{7}$$

$$U_{C_L} = \sqrt{\left(\frac{1}{q_\infty S} U_L\right)^2 + \left(\frac{L}{q_\infty^2 S} U_{q_\infty}\right)^2 + \left(\frac{L}{q_\infty S^2} U_S\right)^2} \tag{8}$$

The relative uncertainty can be expressed as:

$$\frac{U_{C_L}}{C_L} = \sqrt{\left(\frac{U_L}{L}\right)^2 + \left(\frac{U_{q_\infty}}{q_\infty}\right)^2 + \left(\frac{U_S}{S}\right)^2} \tag{9}$$

The uncertainty in drag and the pitching moment can be calculated using a similar process. Equations 1 and 2 show that the lift and drag are functions of normal and axial forces as well as the angle of attack. The uncertainties in lift (U_L) and drag (U_D) can be calculated using equations 10 and 11.

$$U_L = \sqrt{\left(U_{F_N} \cos \alpha\right)^2 + \left(U_{F_A} \sin \alpha\right)^2 + (D U_\alpha)^2} \tag{10}$$

$$U_D = \sqrt{\left(U_{F_A} \cos \alpha\right)^2 + \left(U_{F_N} \sin \alpha\right)^2 + (L U_\alpha)^2} \tag{11}$$

The uncertainty in the pitching moment (U_M) is a function of the moment measured about the balance reference point (U_{Mbal}), the offset between the balance and model reference points (x_{off}),

the uncertainty in this offset distance (U_{xoff}), the normal force, and the uncertainty in the normal force:

$$U_M = \sqrt{\left(U_{M_{bal}}\right)^2 + \left(x_{off}U_{F_N}\right)^2 + \left(F_N U_{x_{off}}\right)^2}$$ (12)

The swept-wing model used in this study was precisely manufactured using a Computer Numerical Control machine, and it will therefore be assumed that the uncertainty in the planform area (U_s) is negligible. The uncertainty in the mean aerodynamic chord (U_{cmac}), used for nondimensionalizing the pitching moment, was also considered negligible. The uncertainty in the angle of attack (U_α) is assumed to be ±0.05°, and the uncertainty in the offset distance between moment reference points (U_{xoff}) is assumed to be ±0.01 in.

Table 2 lists the absolute and relative uncertainties in C_L, C_D, and C_M. The values in table 2 require a reference condition to be selected. For this example, the reference condition was $\alpha = 4°$, which corresponded to $C_L \approx 0.5$ for $Re = 2.4 \times 10^6$.

Table 2. Absolute and relative uncertainties in aerodynamic coefficients

Variable	Reference Value	Absolute Uncertainty	Relative Uncertainty (%)
C_L	0.5029	0.00137	0.272
C_D	0.0215	0.00068	3.15
C_M	-0.0067	0.0006	-9.01

Reference values correspond to $\alpha = 4°$

2.2 SWEPT-WING MODEL

As described in section 1.1, the semispan model fabricated for these wind tunnel tests was based on an 8.9% scale version of the CRM65 wing. The full-scale CRM65 geometry has a realistic cruise configuration loading applied to the wing, resulting in a wing shear similar to dihedral [29]. To simplify the design of the removable leading-edge segments (described below), the shearing or "bending" of the wing was removed from the model geometry, resulting in an unsheared wing with a straight leading edge across the span of the model. The wing retains the twist and taper of the CRM65. Table 3 summarizes the geometric parameters of the wing, and a diagram of the CRM planform is shown in figure 2 with key dimensions. The model was machined from aluminum and contains 219 pressure taps in its clean configuration. The model was specifically designed to interface efficiently with the Wichita State 7 x 10 ft wind-tunnel facility, but the design is also general enough that the model could be installed and tested in other facilities of similar size during potential future studies. Figure 3 contains a computer-aided design (CAD) model of the wing and all of its components along with a photograph of the wing installed in the wind tunnel (with circular splitter plate).

Table 3. Summary of wing geometric parameters

Wing Parameter	Value
Span	5.00' (60.00″)
MAC	1.39' (16.67″)
Area	$6.01'^2$ (865.3^{2}″)
Volume	$0.617'^3$ (1069^{3}″)
Aspect ratio*	8.3
Taper ratio	0.23
Root chord	2.25 ft (27.00″)
Tip chord	0.52 ft (6.19″)
Root α	4.4°
Tip α	-3.8°
1/4-chord sweep angle	35°
Leading-edge sweep angle	37.2°

MAC = Mean Aerodynamic Chord
* Though the other parameters in this table are defined specifically for this model, the aspect ratio is defined for a complete airplane configuration using the formula, $\frac{(2 \; x \; semispan)^2}{2 \; x \; area \; of \; one \; wing}$.
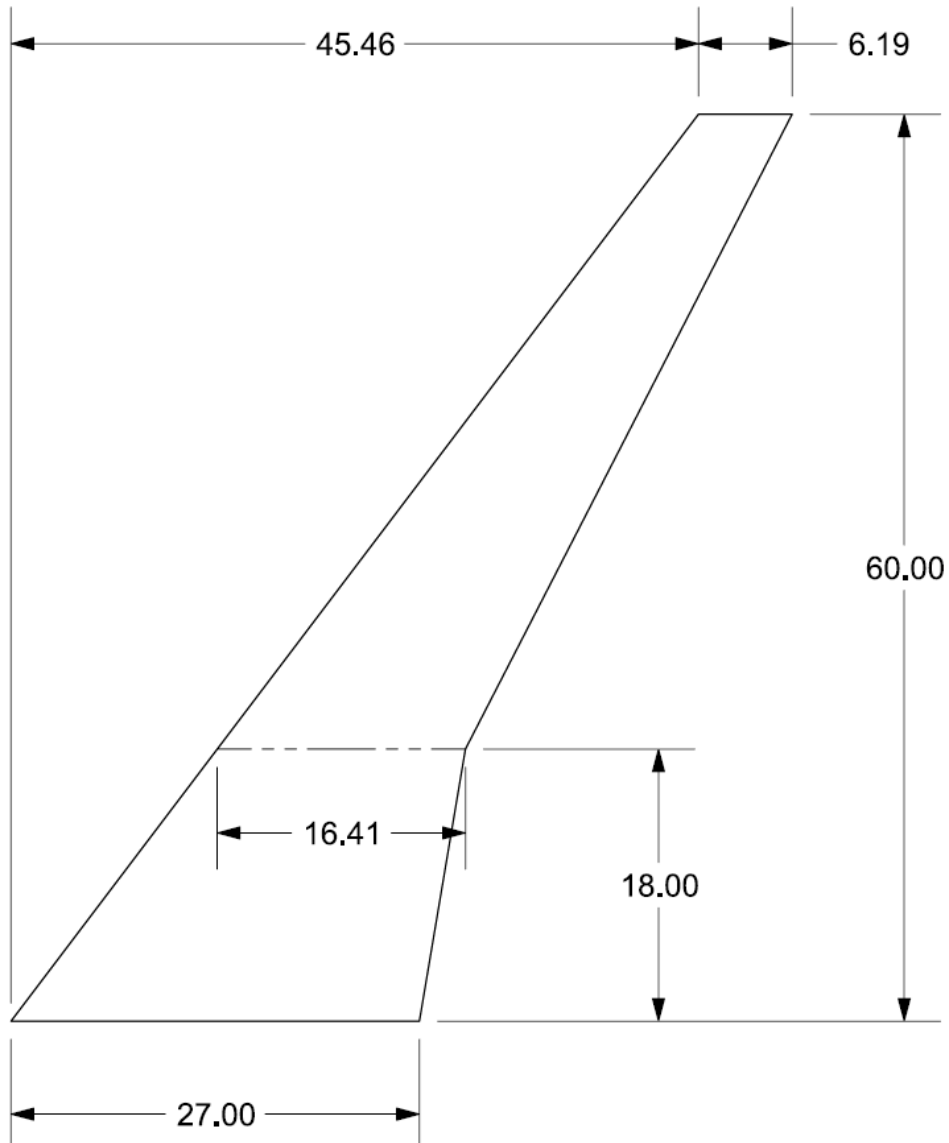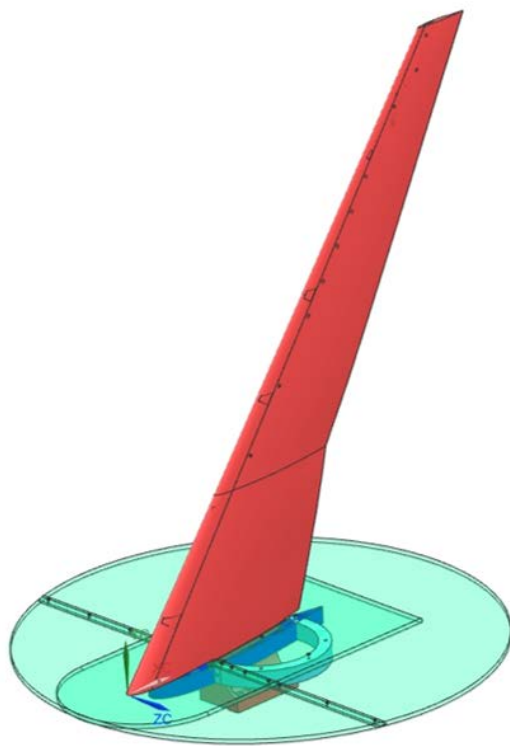
Figure 2. CRM planform with key dimensions labeled in inches

<table>
<tr><td>(a)</td><td>(b)</td></tr>
</table>

Figure 3. The (a) CAD model of wing and (b) wing installed in Wichita State University wind tunnel

A unique feature of this model compared with other aerodynamic models is the removable leading edge (RLE) that allows artificial ice shapes to be added to the wing. This feature allows for very efficient and repeatable changes in the artificial ice-shape configurations. This design is extremely beneficial for this type of research, for which many different ice-shape configurations will be investigated. The machined, aluminum portions of the model consist of the main element (including a spar that attaches to the force balance), a full-span clean leading edge, and a partial-span leading edge used for mounting ice shapes. An open channel exists between the main element and any of the leading-edge components for routing pressure tubing out the base of the model to the data acquisition system. The seam between the clean leading edge and the main element is a straight line on both the upper and lower surfaces, but the seam is not at the same location on both surfaces. Typically, ice accretes farther back on the wing of an aircraft on the lower surface than the upper surface, so the lower surface artificial ice shapes cover a greater portion of the local chord. At the root of the wing, the seam is at 9.3% and 22.8% of the local streamwise chord on the upper and lower surfaces, respectively. At the tip of the wing, the seam is at 14.8% and 40.6% of the local streamwise chord on the upper and lower surfaces, respectively. The seam between components along the upper surface of the model can be seen in figures 3 and 4.

When artificial ice shapes are mounted on the wing for testing, the partial-span RLE is used to attach some of those pieces. The partial-span RLE extends from the root to just beyond half the span of the model, and it contains a portion of the airfoil contour on the lower surface. Artificial ice shapes are attached to this RLE and cover the entire upper surface of the RLE. No pressure

taps were added to this leading edge. Outboard of this partial-span leading edge, the artificial ice shapes were attached directly to the main element. The reason for this is that the model thickness decreases significantly on the outboard portion of the wing. There is not enough material to extend the RLE. This design does not adversely affect the efficiency or repeatability of the artificial ice shape configuration changes. The artificial ice shapes were created using an RPM technique called SLA. A representative ice shape was added to the necessary wing geometry for each segment of wing span. The ice shapes tested during this campaign are discussed in the following section. During these tests, the leading edge was divided into six approximately equal-length segments. Each of the segments consisted of approximately 12.5 in. of the swept leading edge of the wing. Pressure taps were installed in each of these segments at the same locations as on the clean aluminum leading edge. The pressure tap holes were included in the RPM design, and then steel tubes were glued in to each hole and plumbed to the quick disconnect. Each of the separate SLA components is shown in a different color on the full model in figure 4.
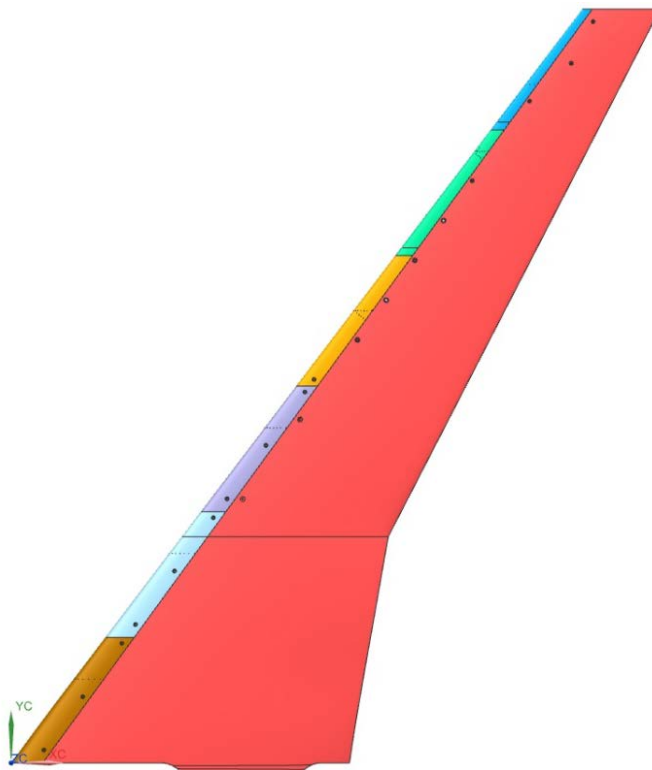

Figure 4. CAD model of wing with each removable leading-edge segment highlighted

The model interfaces with the force balance to acquire aerodynamic data of lift, drag, and pitching moment, but it also contains pressure taps. These taps are placed in 10 different rows on the model. Some rows are oriented normal-to-the-leading edge, and others are in the streamwise direction. The tap rows are identified by the spanwise position of the furthest upstream tap in the row. The spanwise positions of subsequent taps change in the normal-to-the-leading-edge rows. Further information regarding each of the tap rows can be found in table 4, and the tap row locations are shown graphically in figure 5. The streamwise tap rows each contain upper and lower surface taps as well as a tap located at the leading edge of that row. The normal-to-the-leading-edge taps only contain pressure taps on the upper surface, and they do not extend all the way to the leading edge.

The taps closest to the leading edge from the streamwise row would be used to complete the normal row when plotting the data. The taps in the main element of the model are plumbed with stainless steel tubing from their location on the surface out the root of the model. The taps in the leading edge require a more complicated route. The stainless steel tubing in both the clean leading edge and in the RPM ice leading edges transitions to plastic tubing and then connects to a Scanivalve quick disconnect fitting. The use of these fittings allowed relatively quick model reconfigurations between clean and RPM leading edges.

Table 4. Details of the pressure tap instrumentation

Row Identifier	Orientation	Spanwise Location*		Taps in RLE	Upper Surface	Lower Surface	Total Taps
		y/b	inches				
1	Normal	0.11	6.6	3	12	0	12
2	Streamwise	0.11	6.6	13	19	11	31
3	Streamwise	0.28	16.8	13	18	11	30
4	Normal	0.44	26.4	4	16	0	16
5	Streamwise	0.44	26.4	12	18	10	29
6	Normal	0.60	36.0	4	16	0	16
7	Streamwise	0.60	36.0	13	18	10	29
8	Normal	0.81	48.6	4	16	0	16
9	Streamwise	0.81	48.6	13	18	10	29
10	Streamwise	0.90	54.0	3	11	0	11

* Spanwise location is provided for the leading-edge taps for rows 1, 4, 6, and 8 that were oriented normal to the leading edge.
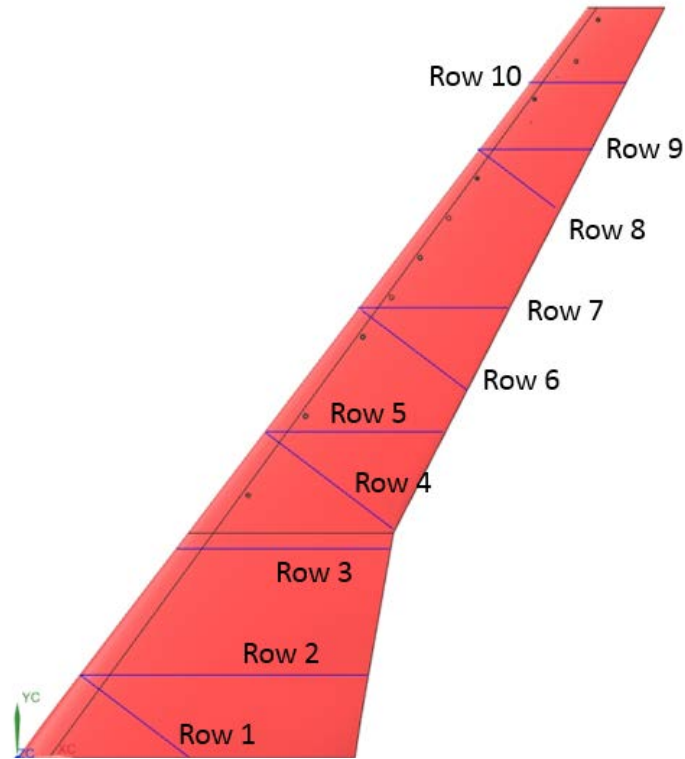
Figure 5. Tap row locations on wing with labels

In addition to the actual wing model, several auxiliary pieces were designed for testing during the first wind-tunnel campaign with this model. As described in section 1.1, a system of splitter plates was developed to evaluate the effect of installation configuration on the wing aerodynamic performance. When testing with a splitter plate, the model is raised out of the wind-tunnel floor boundary layer. A new boundary layer forms on the splitter plate, but the splitter plate geometry is well established and can be repeated in different wind tunnel facilities. The differing floor boundary layers between various wind tunnels should not be a concern when comparing data if a consistent splitter plate is used. The splitter plate system consisted of the splitter plate itself and a shroud that held the splitter plate above the tunnel floor and shielded the model spar from aerodynamic loads. Neither the splitter plate nor the shroud were connected to the model or the force balance. They were mounted to the turntable, so both pieces moved with the model. Two configurations of each of the two components were designed for this test. Each piece had a circular cross-section version that presented a constant geometry even as the angle of attack of the model changed, and each piece also had a smaller, lower blockage version. The smaller splitter plate was generally rectangular, and the smaller shroud was streamlined in shape as a National Advisory Committee for Aeronautics 0018 airfoil. A model of the splitter plates and the wing is shown in figure 6 with each of the components labeled. Both of the splitter plates were designed such that they extended 25% of the root chord thickness upstream of the leading edge of the model. The distance from the center of rotation of the model to the root leading edge sets the diameter of the circular splitter plate. The rectangular plate also extended 25% of the root chord downstream of the root of the model and was five times the maximum root thickness width. For structural reasons, the plates were 0.5-in. thick, and the edges of the plates were rounded. The gap between the bottom of the splitter plates and the wind-tunnel floor was 2 in. based on boundary layer data provided by

16

the WSU facility. Because of the location of the wing spar relative to the center of rotation of the model, the circular shroud had to be relatively large with a diameter of 14.75 in. The blockage from the circular shroud did not change with angle of attack, but the blockage under the splitter plate did change with angle of attack in the streamlined shroud configuration. All of the pieces of the splitter plate system were designed to be removed without affecting the model mounting, so that different configurations could easily be tested. Figure 7 shows the splitter plate system with the key dimensions illustrated. The wing is not shown in figure 7, but the coordinate system indicates the location of the root leading edge. In the case without a splitter plate, the model had to be lowered by 2.5 in. These changes were accomplished using a spacer block between the model spar and the force balance.
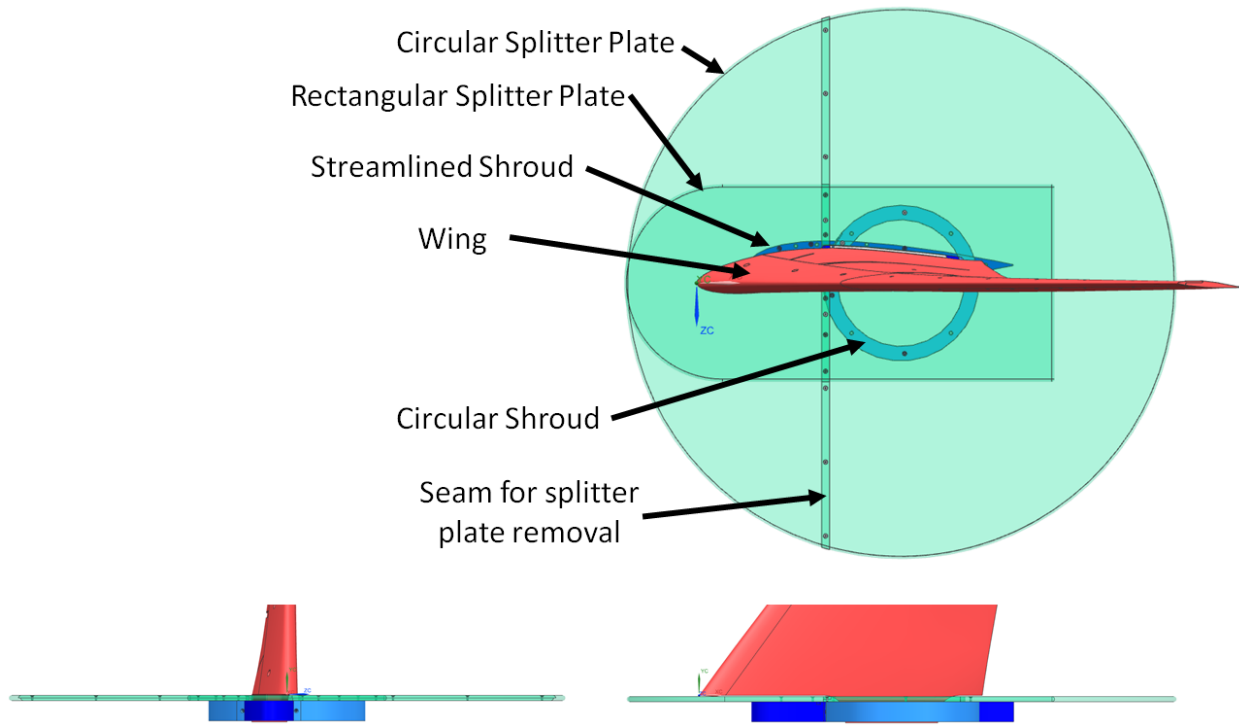

**Figure 6. Multiple model views of the splitter plate system
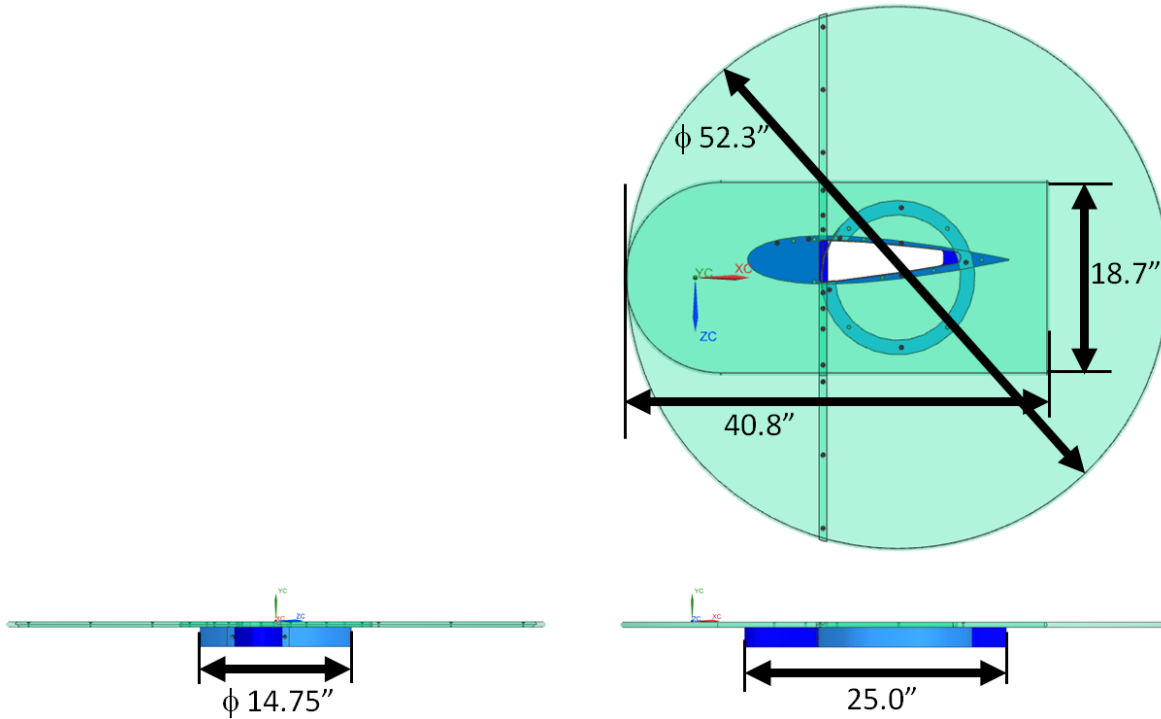and wing with each component labeled**

**Figure 7. Multiple model views of the splitter plate system
without the wing with key dimensions identified**

2.3 ARTIFICAL ICE SHAPE AND ROUGHNESS REPRESENTATIONS

For this wind tunnel campaign, none of the ice shapes or roughness configurations tested were based on actual icing wind-tunnel accretions. Future wind-tunnel tests using this model will include RPM ice shapes based on laser scan data from the IRT at NASA Glenn Research Center [7]. Three models for that wind tunnel were built with full-scale leading edges to represent three different spanwise stations of the CRM65 wing [15]. The model described in the previous section is therefore 8.9% scale of the full-scale reference geometry for this program. This process will allow the ice shapes that are captured at those stations to be extrapolated across the wing to create full-span ice shapes. Those ice shapes will then be scaled down to the appropriate size for this model and tested during future campaigns.

In addition to the clean aluminum machined leading edge, several other leading-edge configurations were created prior to and during this wind-tunnel campaign. As described in section 2.2, six segments along the leading edge could be produced using RPM techniques to represent various potential ice shapes. All of the RPM leading edges were created using SLA and were produced by the company Realize, Inc. [36]. The SLA process uses an ultraviolet laser to solidify liquid polymer resins, and the specific polymer chosen for these components was Accura® 60. Tolerances are advertised to be approximately +/-0.005 in. for this process. The RPM leading-edge segments must be carefully designed to fit over the model easily to minimize the time required to complete ice-shape configuration changes. During this preliminary test, significant time was spent removing material from the RPM shapes so that they would fit properly onto the wing. For efficient testing, future designs must ensure that the RPM shapes fit the wing without superfluous manual

labor. An RPM clean version of the leading edge was produced to quantify the differences between the RPM leading edges and the aluminum leading edge. The tolerances associated with machined aluminum are smaller than the RPM processes, and the RPM leading edges have five seams across the span of the model that are not present in the aluminum leading edge.

In addition, an ice shape that might form on this wing was desired for this preliminary testing. During the course of the design of the models for the IRT, LEWICE3D simulations were performed on the CRM65 [15]. Several icing conditions were simulated during that work, and the one that resulted in the largest horn ice shape was selected for this study. The conditions correspond to $\alpha=3.7°$, $M = 0.36$, static temperature = -4°C, liquid water content = 0.551 g/m^3, median volumetric diameter = 20 µm, and exposure time of 45 minutes. The conditions represented a hold flight phase at 10,000 ft with a pressure of 69.7 kPa. Three of the ice-shape cuts generated from LEWICE3D are shown in figure 8. The section cut of the wing and ice shape is shown at the same scale at each station for perspective regarding the relative size of the ice shapes. These ice-shape sections were lofted into a full-span ice shape using a CAD package, and an example of the result is shown in figure 9 for one of the spanwise segments.
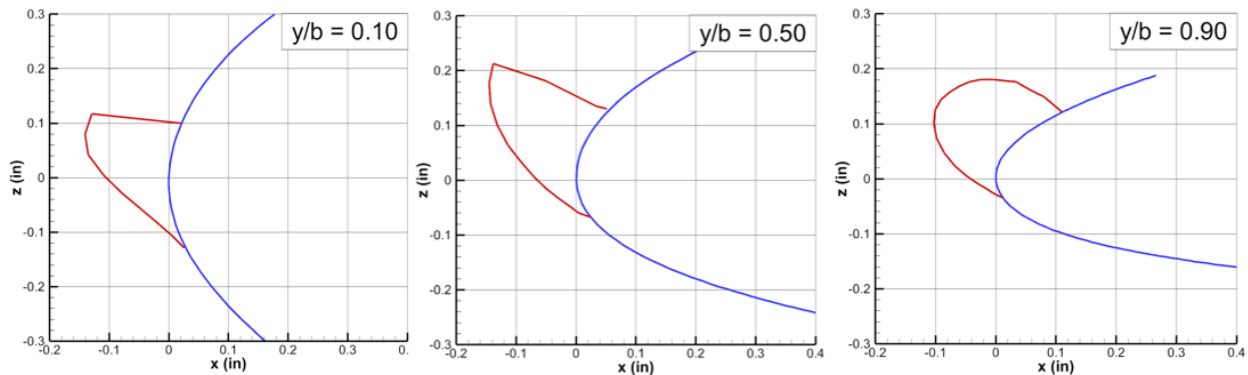

**Figure 8. Plots showing the ice shape generated from LEWICE3D
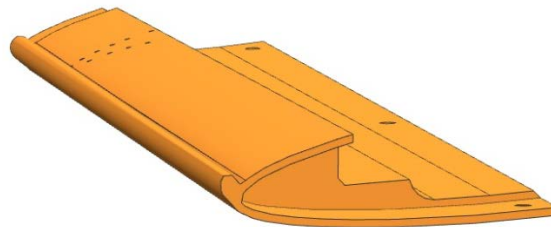and the model section cuts at y/b = 0.1, 0.5, and 0.9**

**Figure 9. CAD model of horn ice shape based on LEWICE3D simulations
added to a leading-edge component**

One of the goals of this test campaign involved understanding the effects of roughness on the wing. Two aspects were involved in this portion of the test. First, the size of the roughness that can accurately be produced using RPM techniques had to be explored, and then the roughness had to be applied to the model to investigate the aerodynamic effects. To simulate ice roughness in the

RPM ice shapes, hemispheres were added to the leading edge of the RPM clean leading edge. The roughness size, k, is the radius of the hemisphere, and a pattern of hemispheres was applied to the leading edge such that the spacing between the center of any two adjacent hemispheres was 1.3 times the diameter of the hemispheres. Figure 10 shows a 2-D illustration of this configuration. The coverage on the upper and lower surfaces was determined using the impingement limits from the previously discussed LEWICE3D simulations, and as the figure illustrates, the roughness covered a greater portion of the lower surface than the upper surface.
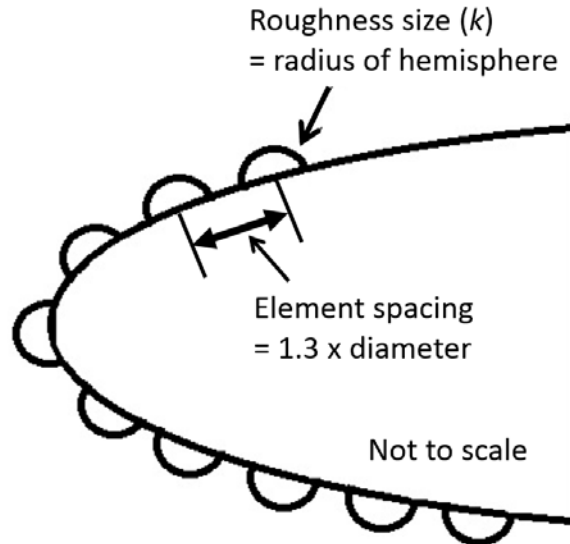

Figure 10. Diagram of hemisphere pattern on leading edge

The CAD pattern of hemispheres on one leading-edge segment is shown in figure 11 along with a close-up view of the roughness pattern. The image on the left shows approximately 7.5 in. of the span, and $k = 0.020$ in. in this case. For reference, the pressure tap holes that are shown have a diameter of 0.050 in After consultation with the SLA manufacturer concerning test articles, it was determined that the smallest hemispheres that could be applied to the entire leading edge had a radius of 0.010 in. A photograph of one of the RPM leading edges with roughness is shown in figure 12.
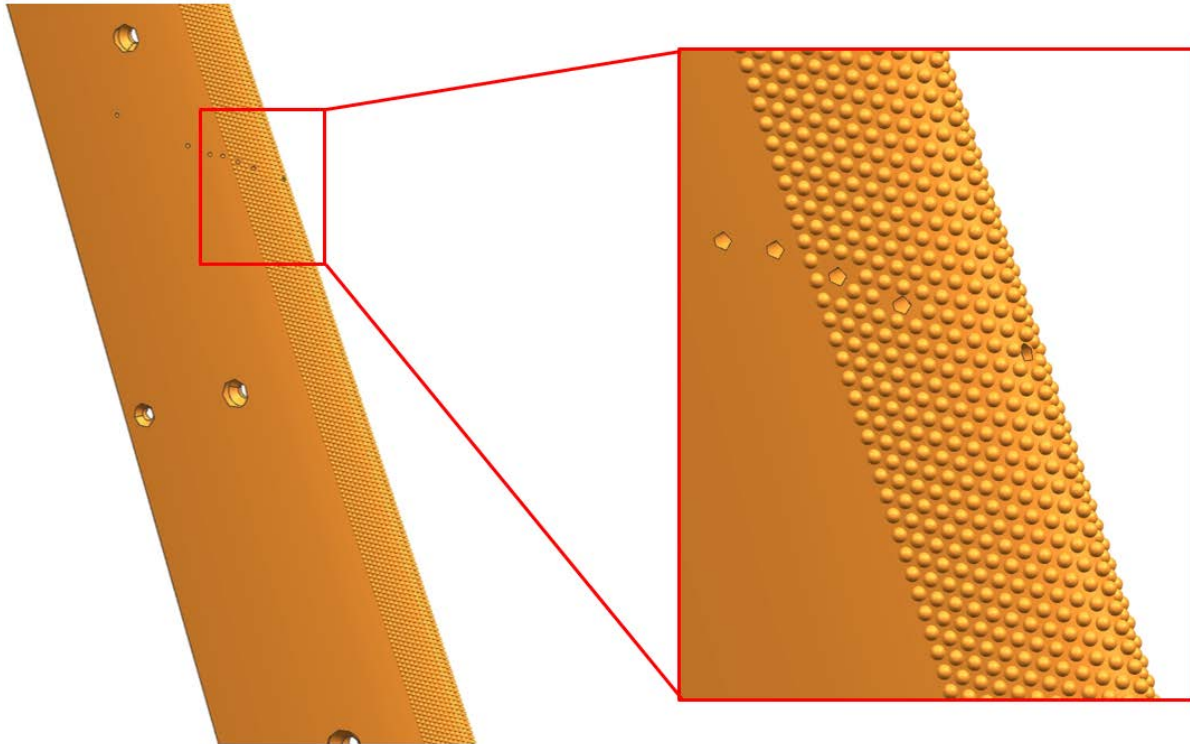
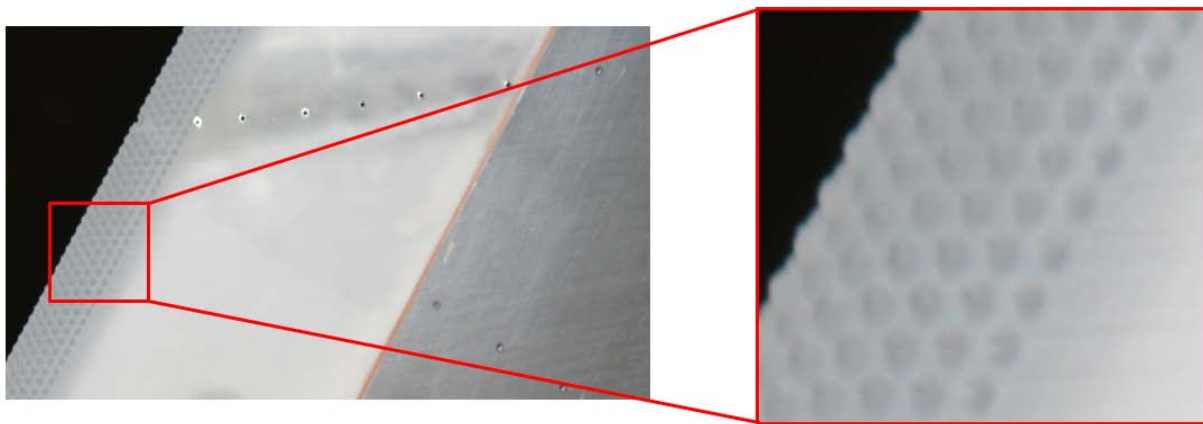**Figure 11. CAD pattern of hemispheres on leading edge**

Figure 12. Photograph of roughness RPM leading edge

Silicon carbide grit was also applied to the leading edge of this model to compare this more traditional roughness simulation process to the results from the RPM roughness simulations. The grit was applied to the model using double-sided tape, and the extent of coverage on the upper and lower surfaces was the same as for the RPM roughness. Plastic templates were created that fit over the leading edge to mark the coverage extent for consistency between the two roughness types. Two different configurations were used with the grit: 1) the entire span was covered with the grit and tape, and 2) gaps were left at the pressure tap rows to acquire that data. Figure 13 contains photographs of the grit on the double-sided tape before and after it was applied to the model.
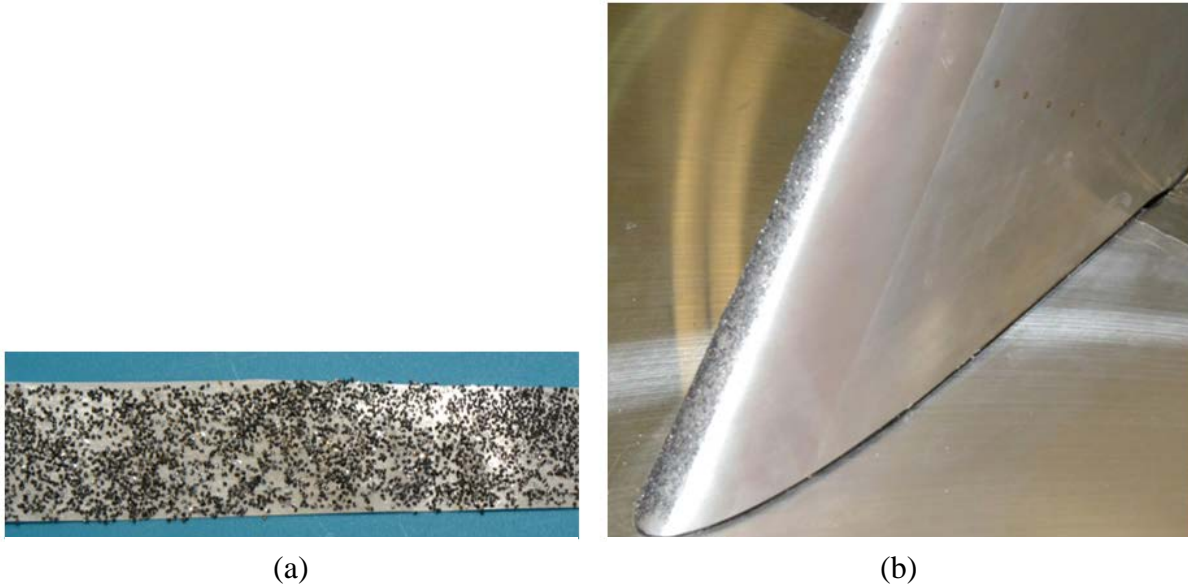
<center>(a)   (b)</center>

Figure 13. Grit on tape (a) before and (b) after being applied to model

The three roughness sizes that were applied to the model during these tests are summarized in table 5. The CRM65 roughness size represents the full-scale size of the roughness feature on the icing model. Elements smaller than that size (0.056 in.) on the IRT model would not be captured at the scale of the model summarized in this work. The table also indicates the type of roughness applied to the model during these tests.

Table 5. Roughness sizes applied to model

CRM65 Roughness Size (inch)	Low-Re Roughness Size (inch)	k/c_{mac}	Application Configuration
0.056	0.005	3.1×10^{-4}	Grit
0.112	0.010	6.3×10^{-4}	RPM/Grit
0.225	0.020	12.5×10^{-4}	RPM/Grit

3. RESULTS AND DISCUSSION

This section presents and discusses the key results of this investigation. Because this work was a preliminary research effort, the data are presented without an extensive analysis of the results. As more data are acquired in future planned test campaigns, these data can be revisited for further analysis. The clean wing results are presented first, followed by the results for the wing with artificial ice roughness and for the one artificial ice shape examined in this effort.

3.1 CLEAN WING

3.1.1 Model Installation Configurations

As described in section 2.2, the CRM wing model was designed with interchangeable splitter plates and shrouds. The model was also able to be mounted flush with the floor of the wind-tunnel test section. The splitter plate configurations were designed based on previous work by Diebold et al. [30]. Figure 14 shows a comparison of lift, drag, and pitching moment for the four configurations acquired at $Re = 2.4 \times 10^6$ and $M = 0.27$. For angles of attack below stall (less than 13.2°), there was virtually no difference in the coefficients of lift and drag. There were slightly larger differences in pitching moment among the various configurations. In the range of $4 < \alpha < 13°$, the configuration with the wing mounted directly at the test-section floor (No Splitter, No Shroud) had a lower C_M than the other three configurations. This was likely the result of the wing root directly interacting with the floor boundary layer. Figure 15 shows a comparison of surface pressure coefficients from the streamwise row of taps closest to the wing root (Row 2, $y/b = 0.11$) at $\alpha = 10.1°$. There is clearly reduced suction pressure on the wing upper surface on the forward half of this section for the "No Splitter, No Shroud" configuration. This reduced suction pressure is likely responsible for the slightly lower C_M at this angle of attack.
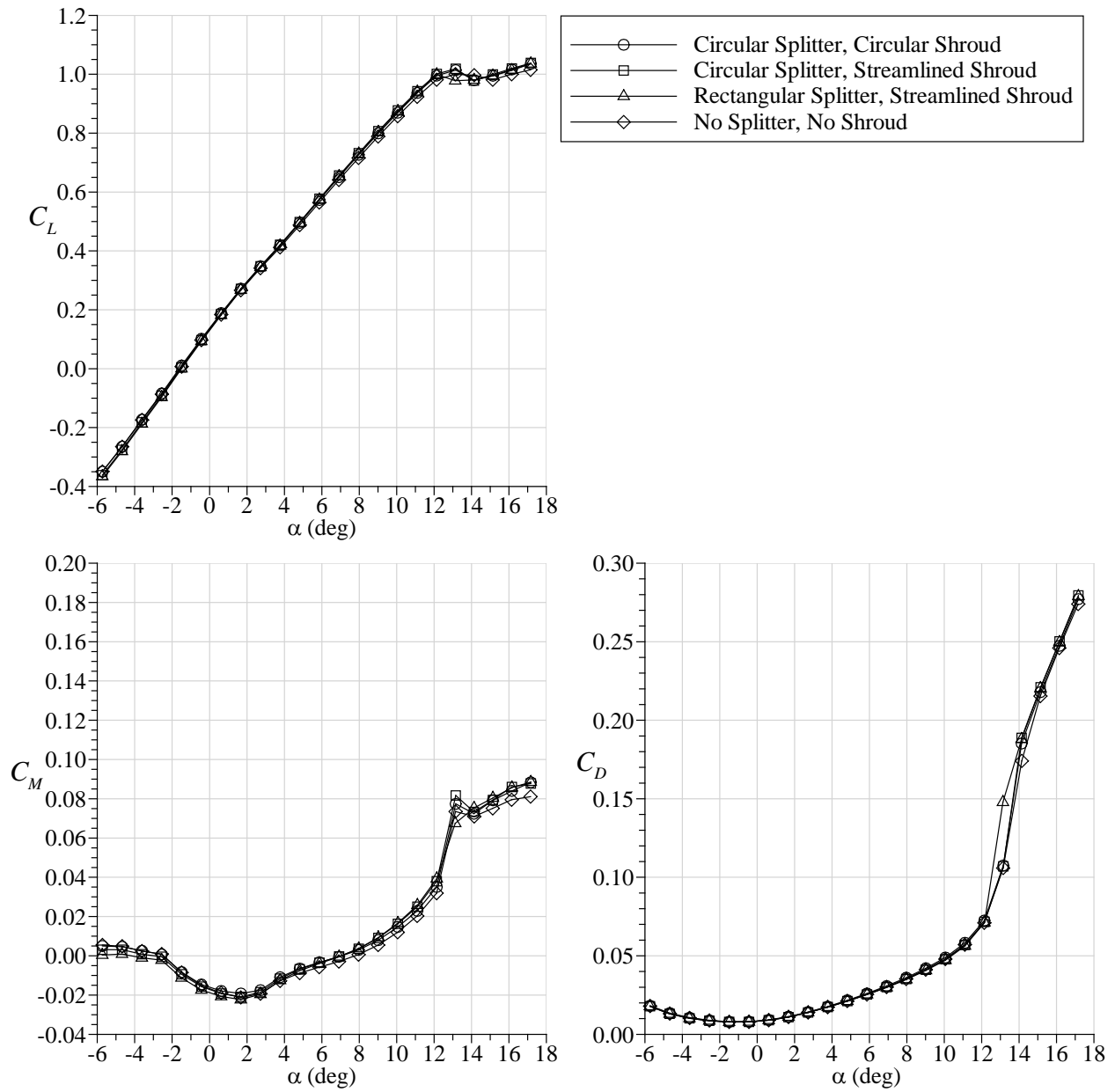
Figure 14. Effect of model installation configuration on clean wing performance at $Re = 2.4 \times 10^6$ and $M = 0.27$
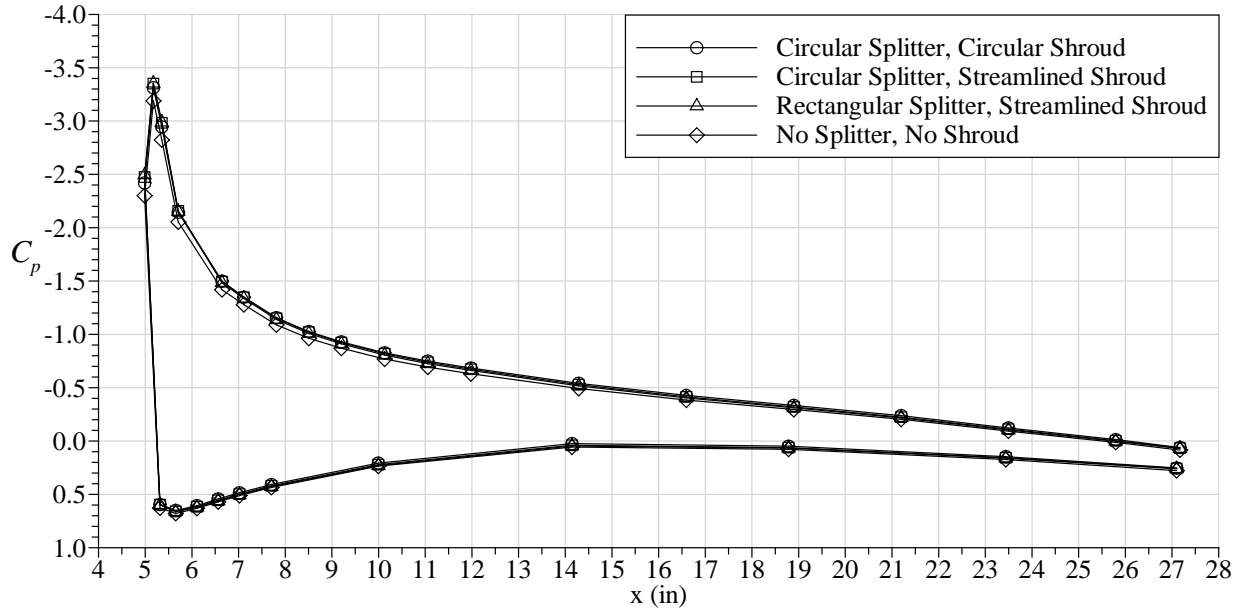
Figure 15. Effect of model installation configuration on clean wing surface pressure distribution at $Re = 2.4 \times 10^6$ and $M = 0.27$, ROW 2, $y/b = 0.11$, $\alpha = 10.1°$

The performance data in figure 14 show more significant differences among the various configurations at the stalling angle of attack, $\alpha = 13.2°$. At this angle of attack, the configuration with the Rectangular Splitter and Streamlined Shroud exhibited the largest difference in performance from the other three. Surface pressure data on the streamwise tap row near the midspan station (row 5, $y/b = 0.44$) are plotted for this angle of attack in figure 16. These data clearly show that the wing was stalled for the Rectangular Splitter and Streamlined Shroud configuration, and the wing was installed for the other three configurations. Similar behavior was noted for streamwise pressure rows from row 3 ($y/b = 0.28$) to row 7 ($y/b = 0.60$). Pressure data outboard of row 7 ($y/b = 0.60$) indicated that the wing was stalled for all four configurations.
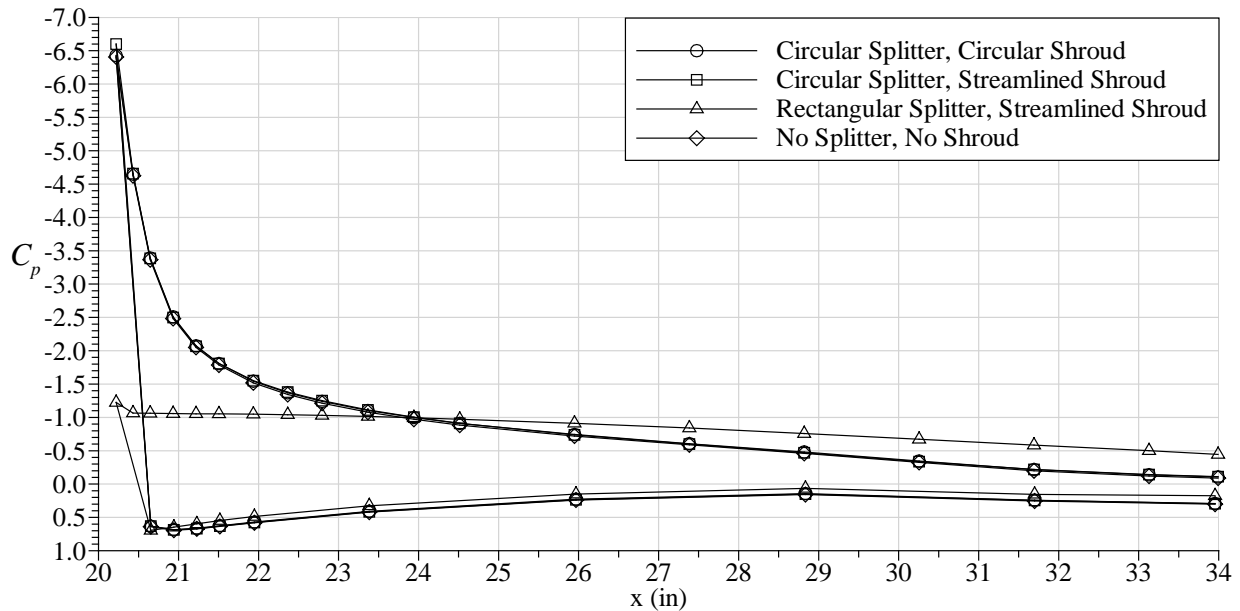
Figure 16. Effect of model installation configuration on clean wing surface pressure distribution at $Re = 2.4 \times 10^6$ and $M = 0.27$, ROW 5, $y/b = 0.44$, $\alpha = 13.2°$

Data like these were generated for the other two Re and M conditions and the comparisons for lift and drag were virtually identical to that shown in figure 14. There was more variation in pitching moment for the various configurations at the other Re and M conditions. This variation was not considered significant with respect to the selection of a final model installation configuration for these experiments.

An analysis of these data led to the selection of the installation configuration using the circular splitter plate combined with the streamlined shroud. As cited in this section, there were some anomalies associated with rectangular splitter plate that led to this being eliminated as a possible configuration. The mounting of the wing directly at the test section floor (No Splitter, No Shroud) was also eliminated for similar reasons. In addition, this installation would likely render the data unique to this wind-tunnel facility because of the direct influence of the floor boundary layer. The installation using the circular splitter plate along with the circular shroud yielded aerodynamic performance results that were very similar to the circular splitter plate coupled with the streamlined shroud. The streamlined shroud was selected because it likely resulted in minimal flow separation in the region between the test-section floor and the splitter plate. This was considered desirable for any future research involving a detailed CFD model of the wing and installation configuration. Therefore, the remainder of the data presented in this report is for the wing installed with the circular splitter plate coupled with the streamlined shroud.

3.1.2 Reynolds and Mach Number Effects

As noted in section 2, the WSU wind tunnel operates near atmospheric pressure. Therefore, the Reynolds and Mach numbers cannot be controlled independently. The conditions were selected to yield a two-fold and three-fold increase in both Reynolds number and Mach number from the lowest condition. The aerodynamic performance results for the clean wing at these conditions are

26

plotted in figure 17. For these cases, the angle of attack resolution was increased in stall region based on the $Re = 1.6 \times 10^6$ and $M = 0.18$ condition. As shown in figure 17 for this condition, wing stall was well defined by an abrupt change in all three performance coefficients between $\alpha = 13.9°$ and $14.1°$, with $C_{L,max} = 1.04$ at $\alpha_{stall} = 13.9°$.
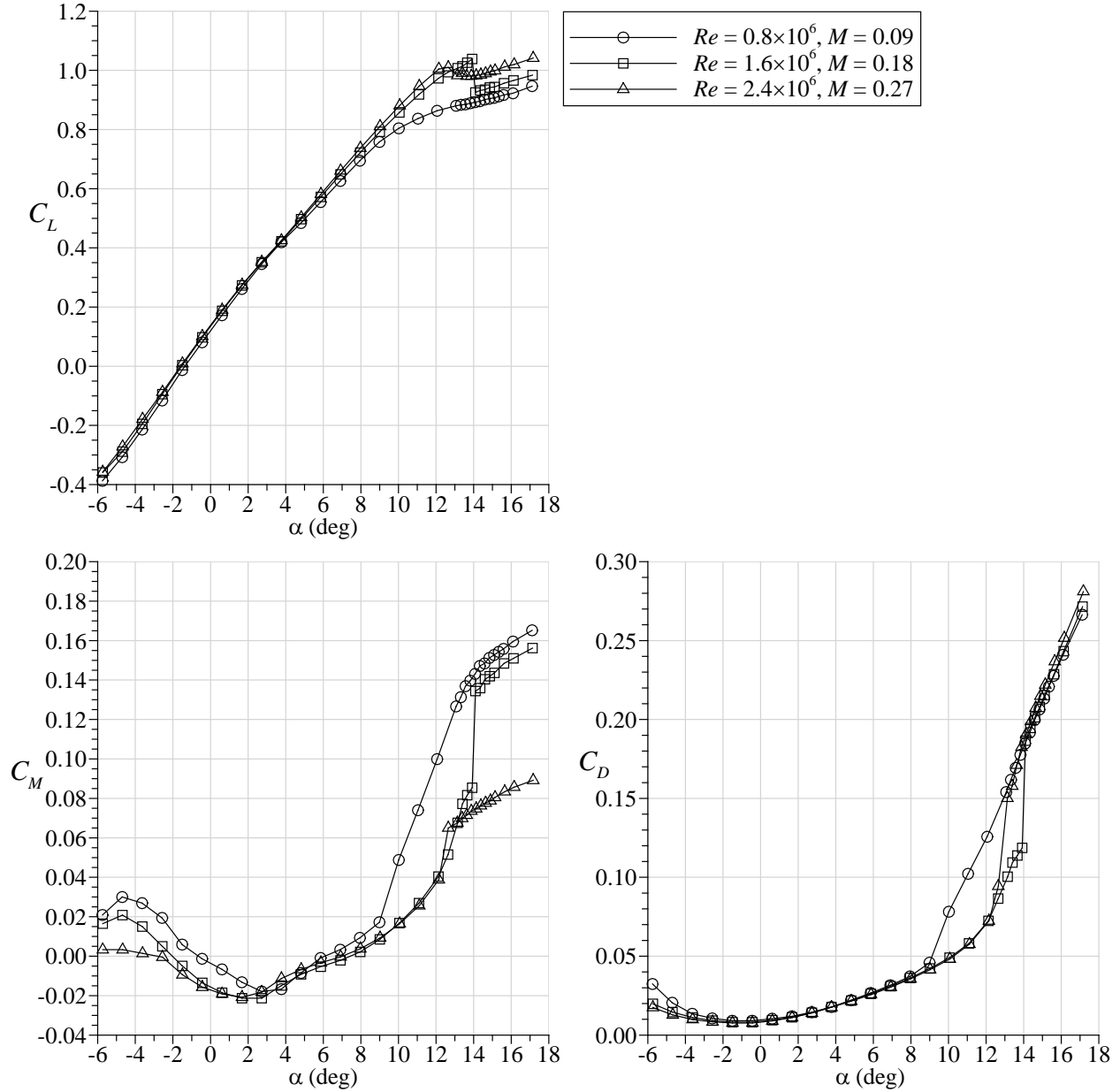

Figure 17. Effect of Reynolds and Mach number on clean wing performance

The same interval of increased angle of attack resolution was also used for the other two conditions. At the highest Reynolds and Mach number condition, the changes in the performance coefficient were less abrupt, but stall was still well defined with $C_{L,max} = 1.01$ at $\alpha_{stall} = 12.7°$. At the lowest Reynolds and Mach number condition, wing stall occurred at a much lower angle of attack based on the large changes in C_M and C_D between $\alpha = 9.0°$ and $10.0°$. There was also a

distinct change in the lift-curve slope between these angles of attack. For this condition, the interval of increase angle of attack resolution was in the post-stall region. This interval was not adjusted for subsequent runs because of a lack of time to complete the experiments.

The wing stall for $Re = 0.8 \times 10^6$ and $M = 0.09$ was characterized by a significant loss of leading-edge suction pressure on the outboard portions of the wing between $\alpha = 9.0°$ and $10.0°$. This is shown in figure 18 with the surface pressures for the streamwise pressure rows at $y/b = 0.28$, 0.44, and 0.60. On the inboard portion of the wing at $y/b = 0.28$, there were only minor differences in the change in pressure coefficient going from $\alpha = 9.0°$ to $10.0°$. This is contrasted with the comparisons at $y/b = 0.44$ and 0.60, where the wing is clearly stalled at the higher angle of attack. This resulted in the large changes in C_M and C_D observed in figure 17.
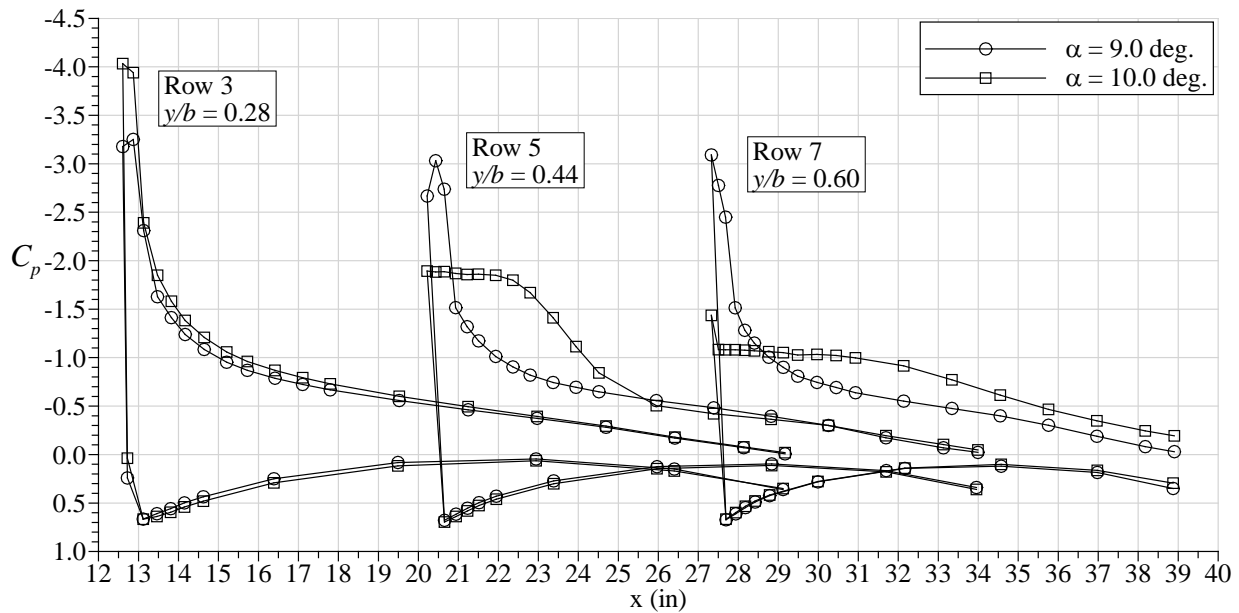

Figure 18. Comparison of clean wing surface pressure distribution at $Re = 0.8 \times 10^6$ and $M = 0.09$

A similar comparison of surface pressure is presented in figure 19 for $Re = 1.6 \times 10^6$ and $M = 0.18$ over the stall region from $\alpha = 13.9°$ and $14.1°$. For this condition, the wing stall also occurred on the inboard portion of the wing, but between $y/b = 0.11$ and 0.28. This stall location is farther inboard than for the lower Reynolds and Mach number condition in figure 18. The additional loss in lift on this inboard portion of the wing likely contributed to the abrupt drop in C_L observed in figure 17.
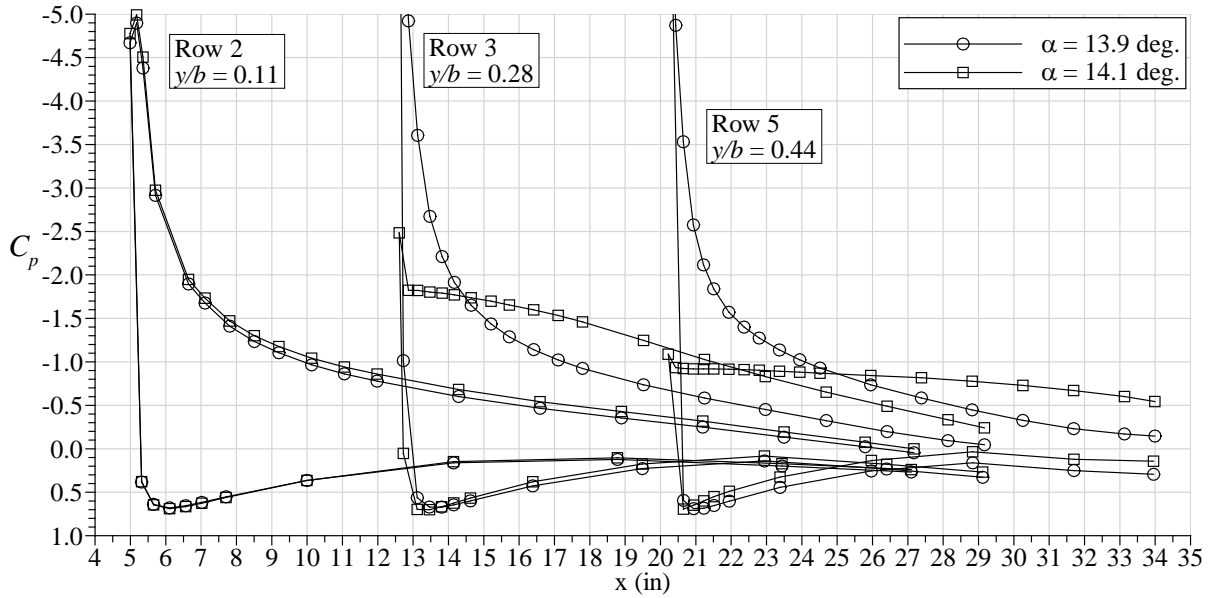
**Figure 19. Comparison of clean wing surface pressure distribution
at $Re = 1.6 \times 10^6$ and $M = 0.18$**

This analysis was also performed in figure 20 for $Re = 2.4 \times 10^6$ and $M = 0.27$ over the stall region from $\alpha = 12.6°$ and $13.1°$. For this condition, the results were more similar to the lowest Reynolds and Mach number condition where the wing stall occurred on the portion of the wing between $y/b = 0.28$ and 0.44. As with that case, maintaining the lift over a larger portion of the inboard wing was likely responsible for the less abrupt change in C_L between these two angles of attack.
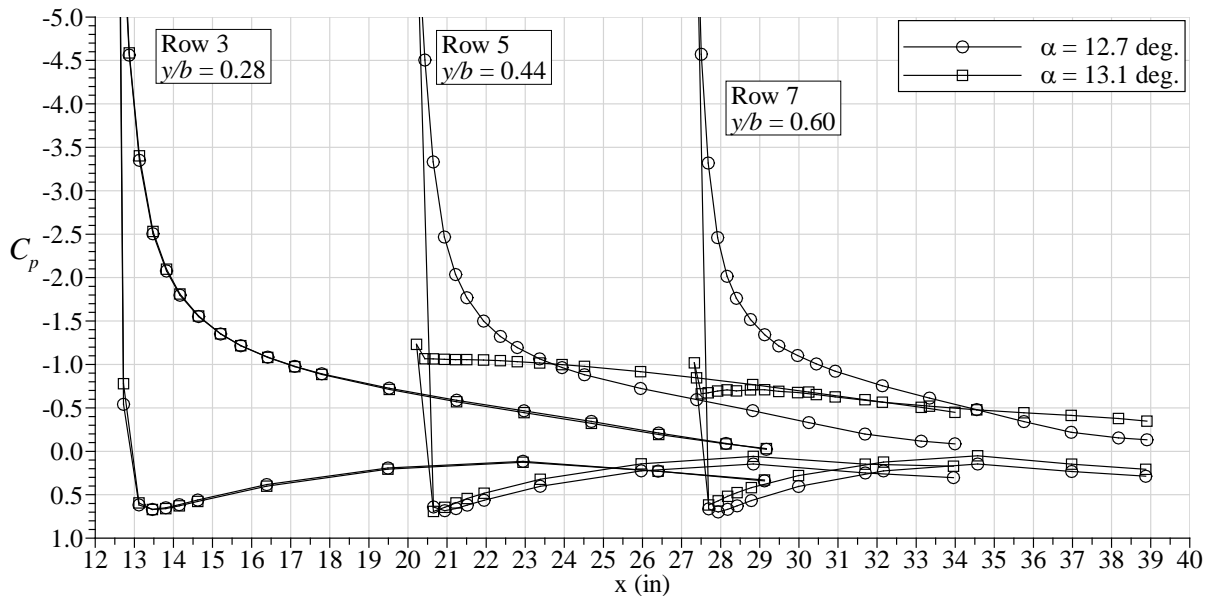

**Figure 20. Comparison of clean wing surface pressure distribution
at $Re = 2.4 \times 10^6$ and $M = 0.27$**

29

Some basic observations on these Reynolds and Mach number effects can be made through further comparison of surface pressure. For example, these data are plotted in figure 21 for all three conditions at the stalling angle of 9.0° associated with the $Re = 0.8 \times 10^6$ and $M = 0.09$ condition at Row 9 near the wing tip ($y/b = 0.81$). For this case, the wing tip region has already begun to stall, whereas there appears to be minimum separation for the higher Reynolds and Mach number conditions.
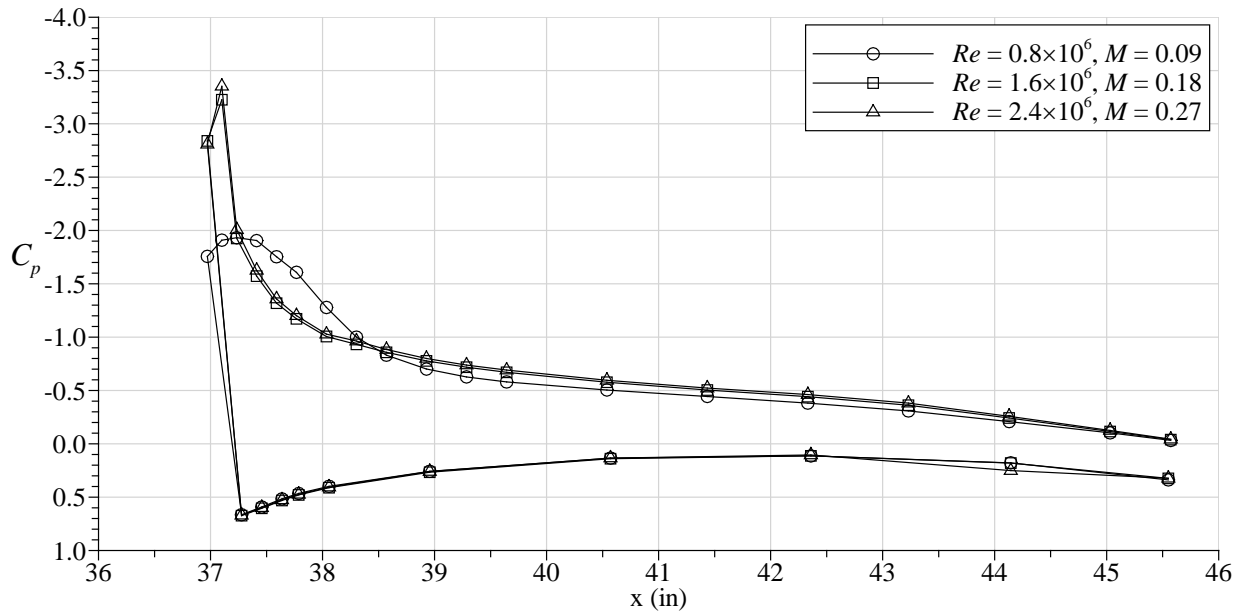

Figure 21. Effect of Reynolds and Mach number on clean wing surface pressure distribution at Row 9, $y/b = 0.81$, $\alpha = 9.0°$

Further comparison in surface pressure was performed for the two higher Reynolds and Mach number conditions at the stalling angle of attack of 12.7° associated with $Re = 2.4 \times 10^6$ and $M = 0.27$. These data are shown in figure 22 for pressure Row 7 at $y/b = 0.60$. The other pressure rows exhibited similar comparisons. There were only minor differences in the pressure coefficient on the upper surface of the wing with slightly higher suction pressures observed for the higher Reynolds and Mach number.
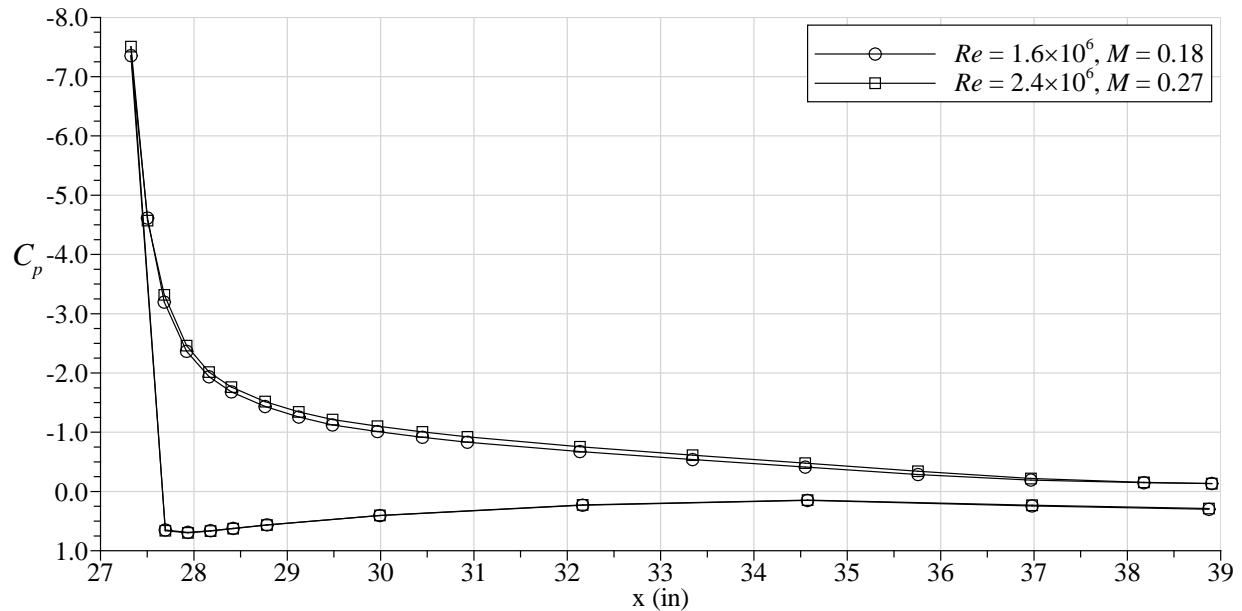
Figure 22. Effect of Reynolds and Mach number on clean wing surface pressure distribution at row 7, *y/b* = 0.60, α = 12.7°

The effects of Reynolds number and Mach number on the swept-wing performance include all of the typical parameters for straight wings, such as boundary-layer transition and separation and compressibility. The additional variables associated with this wing are complicated by a number of factors including the large amount of sweep (37.2° at the leading edge), high taper ratio (0.23), and twist. These variables in turn affect the evolution of boundary-layer transition, separation, and compressibility effects. Therefore, the analysis of Reynolds number and Mach number effects is limited for this preliminary report. Results from pressure-tunnel tests in the ONERA F1 facility will provide much better insight.

3.1.3 Flow Visualization

Surface oil flow visualization was performed using the method described in section 2.1. All of the flow visualization was conducted using the circular splitter plate and streamlined shroud configuration, and the majority of images were acquired at a Reynolds number of 1.6×10^6 and Mach number of 0.18. As such, all of the images discussed in this section show the clean model at those conditions. The images shown in figure 23 show the flow on the wing before the stall process begins (α = 9.0°) and as the stall progresses on the model (α = 13.1° and 15.1°). For the case of α = 9.0°, the flow appears to separate near the leading edge, forming a small spanwise leading-edge vortex that reattached to the model, and remained attached across the rest of the span. This interpretation of the flow visualization is consistent with the lift coefficient data shown in figure 17. At higher angles of attack, the leading-edge vortex failed to reattach to the model resulting in a stalled portion of the wing. The leading-edge vortex moved inboard between the α = 13.1° and 15.1° cases and is labeled on those two images in figure 23. Identification of stall for the entire wing is challenging and not well defined. Simply because a portion of the wing is stalled does not necessarily imply that the entire wing is stalled. The surface pressure data are consistent with these oil flow images as shown in figure 24. The pressure coefficient is shown for three pressure rows

31

representing y/b = 0.28, 0.60, and 0.81 for the three angles of attack shown in the oil flow images. At α = 9.0°, none of the pressure rows indicate stall. At α = 13.1°, the pressure row at y/b = 0.81 indicates stall, and at α = 15.1°, all three pressure rows shown indicate stall.
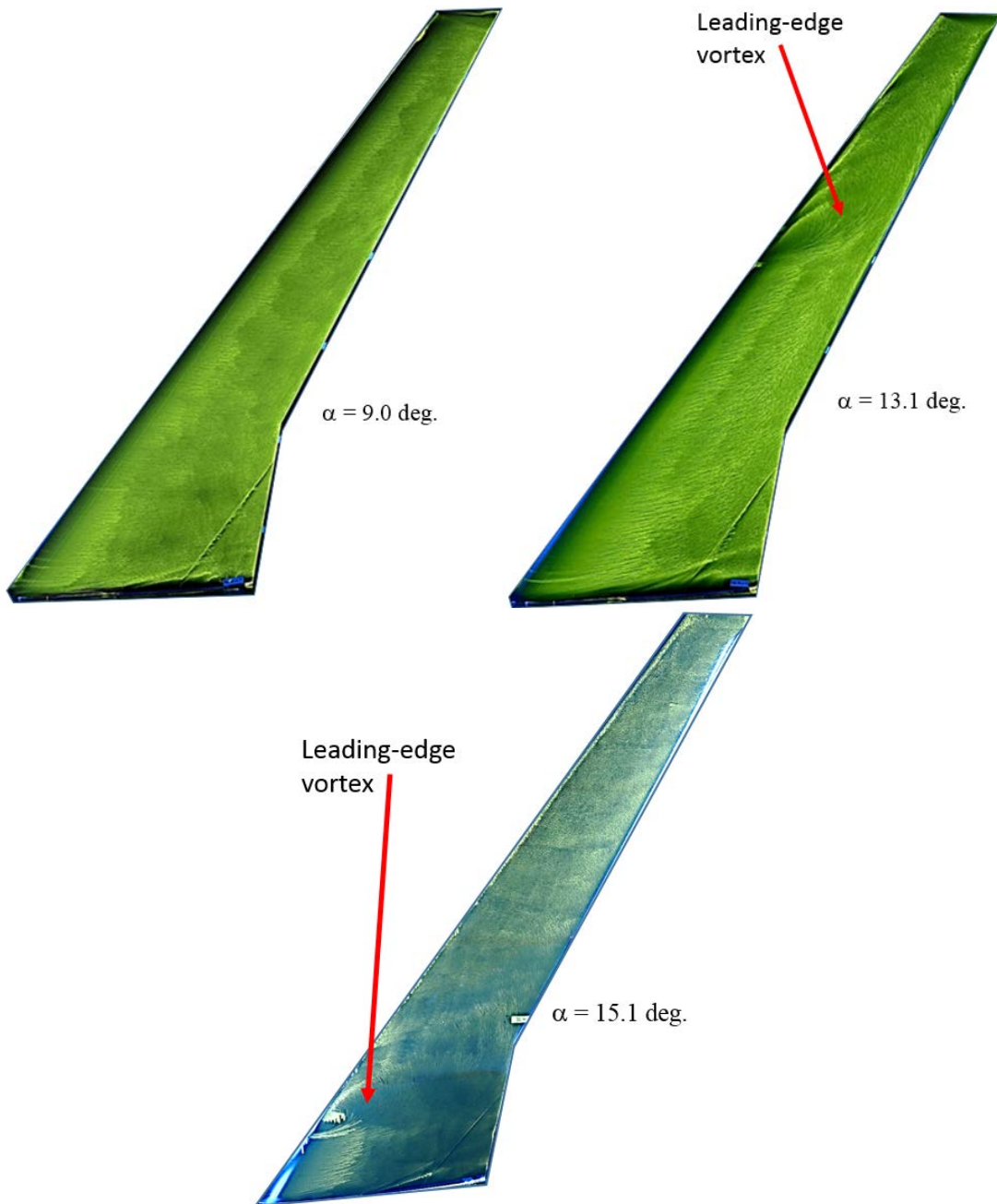

Figure 23. Surface oil flow visualization comparison for the clean wing at Re = 1.6 × 10⁶ and M = 0.18
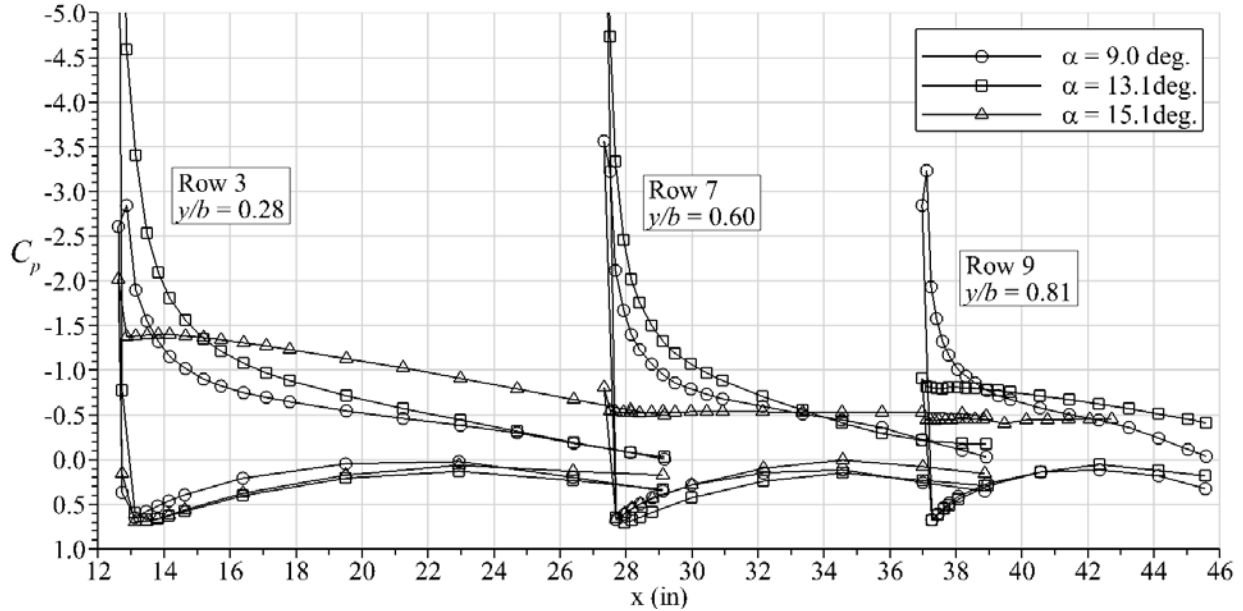
**Figure 24. Comparison of clean wing surface pressure distribution
at $Re = 1.6 \times 10^6$ and $M = 0.18$**

3.2 ICED WING

This section presents the aerodynamic results for the wing configured with artificial ice roughness and one artificial ice shape. Comparison of these effects is first shown in section 3.2.1 followed by a discussion of Reynolds and Mach number effects in section 3.2.2. The results are organized in this way because the effects of Reynolds and Mach number on the iced-wing performance were very small. As noted in section 3.1.1, all of the data in this section were acquired with the circular splitter plate coupled with the streamlined shroud.

3.2.1 Effect of Artificial Ice Roughness and Ice Shape

The various artificial roughness and ice shape configurations described in section 2.3 were installed on the wing and subjected to aerodynamic performance testing at the three Reynolds and Mach number conditions used for the clean wing studies. An RPM version of the clean leading-edge profile was also available as an additional configuration. This was tested to ensure that there was no adverse aerodynamic effect associated with the mechanical installation of the RPM sections to the wing in place of the clean, aluminum leading-edge section (see section 2.3). All of the data shown here are for the $Re = 1.6 \times 10^6$ and $M = 0.18$ condition, because the effects of Reynolds and Mach number were typically very small (see section 3.2.2).

Artificial ice roughness was modeled as a regular pattern of equally sized and spaced hemispheres and fabricated by means of RPM. Two roughness sizes were fabricated and tested this way: $k = 0.010$ in. and $k = 0.020$ in., where k is the height of the roughness measured from the wing surface. The aerodynamic performance results are shown in figure 25 along with the clean wing baseline and the clean wing geometry manufactured by means of RPM. At the outset, it was expected that the performance for the clean wing baseline and the RPM clean leading edge should match exactly, this being the objective for the fabrication process followed. The results were

consistent over the interval -3 < α < 13°. There were some significant differences in the performance coefficients near stall and in the post-stall regimes. An analysis of the data in figure 25 showed that the stall angle was 13.7° for the RPM clean leading edge versus 13.9° for the clean wing baseline. An exact match in the post-stall behavior of these two configurations may be unrealistic given the abrupt stalling characteristics of this wing at this condition. The adverse aerodynamic effect of the artificial roughness is clearly observed in figure 25 and is very distinct from the effects observed for both clean-wing configurations. Therefore, it can be concluded that this adverse aerodynamic effect was due to the artificial roughness as opposed to any effect of the RPM leading-edge configuration itself.
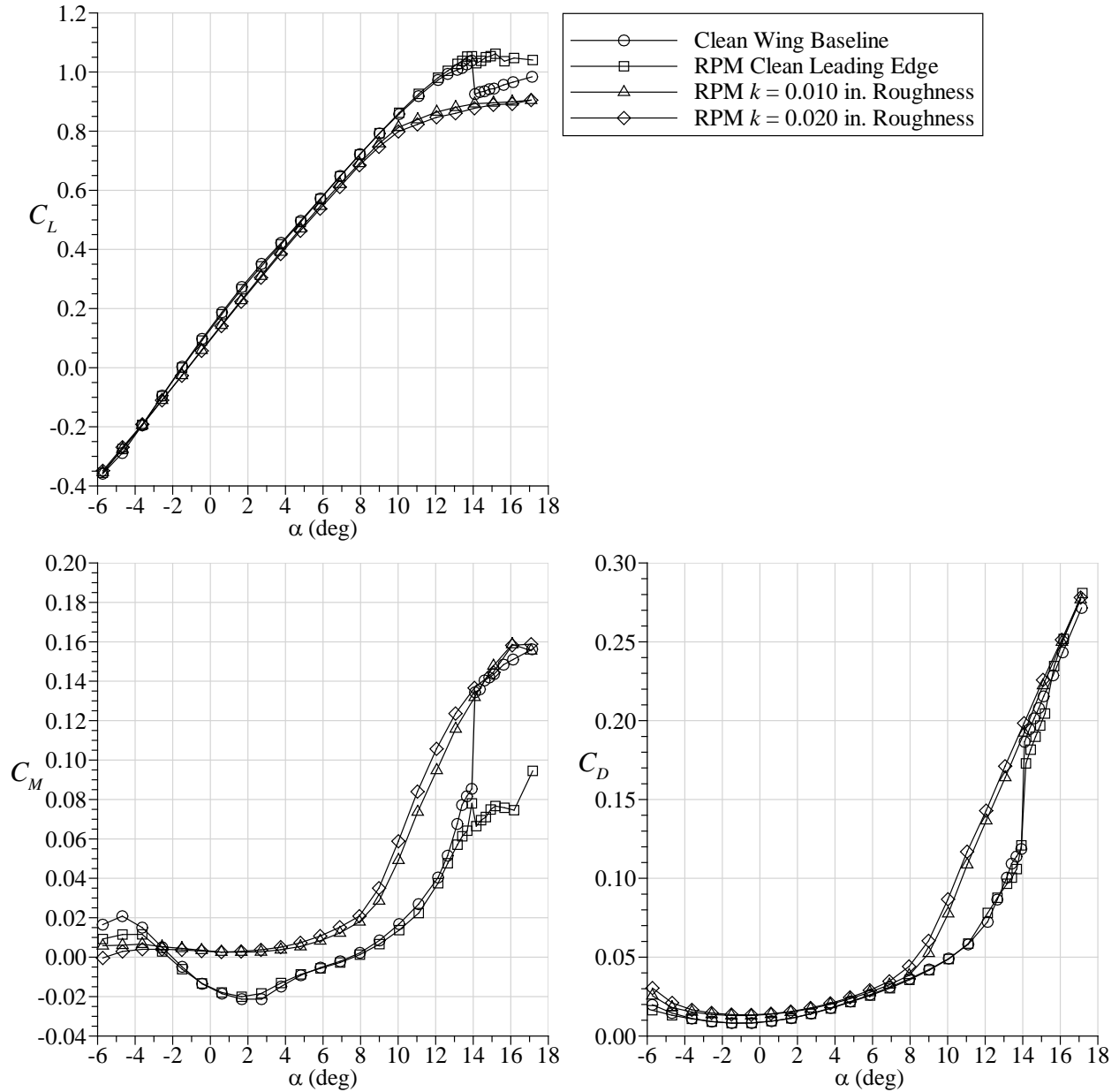

Figure 25. Effect of RPM-based artificial ice roughness on wing performance at $Re = 1.6 \times 10^6$ and $M = 0.18$

Figure 25 also shows the effect of the two artificial roughness sizes on the wing aerodynamic performance. The trends in the data were consistent with typical effects, in which the larger roughness size generally resulted in lower C_L, higher C_D, and lower C_M. From these data, it is difficult to unambiguously identify the angle of attack at which the wing stalls. A logical choice for both roughness sizes is $\alpha_{stall} = 7.9°$, because there is distinct change in the slope of the performance curves, particularly in C_M and C_D. The corresponding $C_{L,max}$ is 0.69 for $k = 0.010$ in. and 0.68 for $k = 0.020$ in.

Aerodynamic tests were also conducted using silicon carbide grains to represent ice roughness. The grit sizes were selected to approximately match the roughness heights used for the RPM-based configurations. Of course, the geometric morphology of silicon carbide grains tends to be "crystalline" or "faceted," which is significantly different from the hemispherical geometry of the RPM-based roughness. In addition to this difference, the grit sizes represent some distribution whereas the RPM-based roughness was uniform in size. Because of these differences, it was not expected that the performance of the grit-based roughness would exactly match that of the RPM-based roughness. These methods simply represent two different approaches to simulating actual ice roughness, which is neither completely hemispherical nor "faceted," but does have some distribution of sizes.

Aerodynamic results for three different grit sizes applied to the wing leading edge are shown in figure 26. For these tests it should be noted that there were spanwise gaps or breaks in the roughness near the pressure tap locations to allow for the measurement of surface pressure as described in section 2.3. In the case of the grit roughness, one additional size of $k = 0.005$ in. was also tested. As for the RPM-based roughness (see figure 25), the stall angle could be chosen as $\alpha_{stall} = 7.9°$, because there was distinct change in the slope of the performance curves, particularly in C_M and C_D. At this angle of attack and lower, the trends in the data were consistent with typical effects where the larger roughness size generally resulted in lower C_L, higher C_D, and lower C_M. For angles of attack higher than 10°, these trends no longer prevail, and the post-stall behavior becomes very difficult to interpret for each of the three configurations.
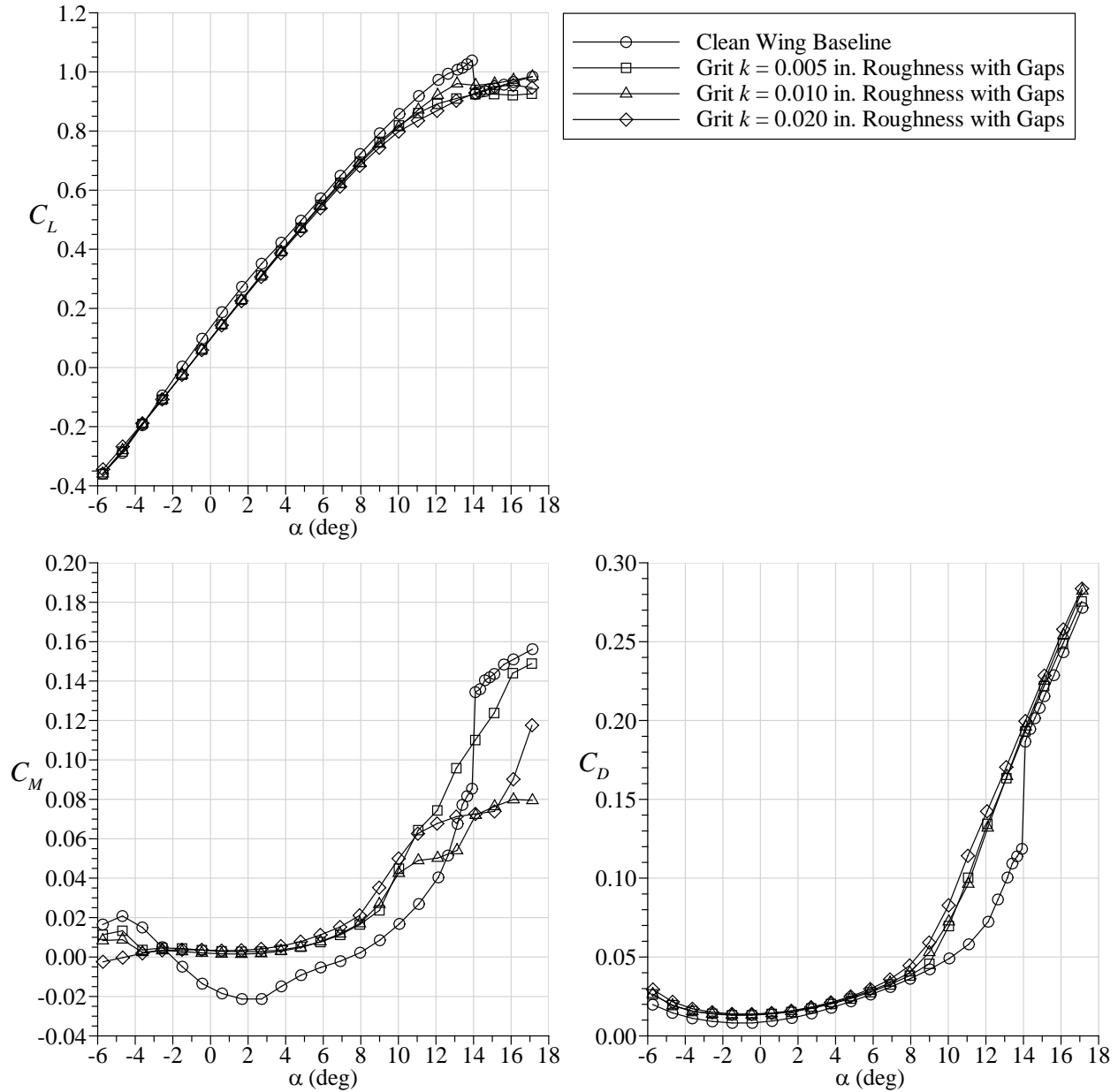
Figure 26. Effect of grit-based artificial ice roughness on wing performance at $Re = 1.6 \times 10^6$ and $M = 0.18$

Further insight into these data was gained by performing a direct comparison of the performance effects of the RPM- and grit-based roughness (see figure 27) for the $k = 0.010$-in. size. An additional configuration plotted in figure 27 is the grit-based roughness without any spanwise gaps at the pressure rows. For this configuration, there was a continuous spanwise extent of grit roughness from root-to-tip, which is a much better match to the RPM-based roughness. This has the disadvantage of covering the pressure taps. These data showed good agreement among the three different roughness simulations up to the stalling angle of attack at 7.9° where the post-stall behavior was different. In the post-stall region, the trends in the data matched much better between the RPM-based roughness and the grit-based roughness with no spanwise gaps. This indicated that

the spanwise gaps used for the grit-based roughness in figure 26 may have contributed to the anomalous post-stall behavior. It was concluded that the wing performance could be very sensitive to spanwise discontinuities in the leading-edge region, and this should be an important factor in the design of artificial ice shapes for future test campaigns.
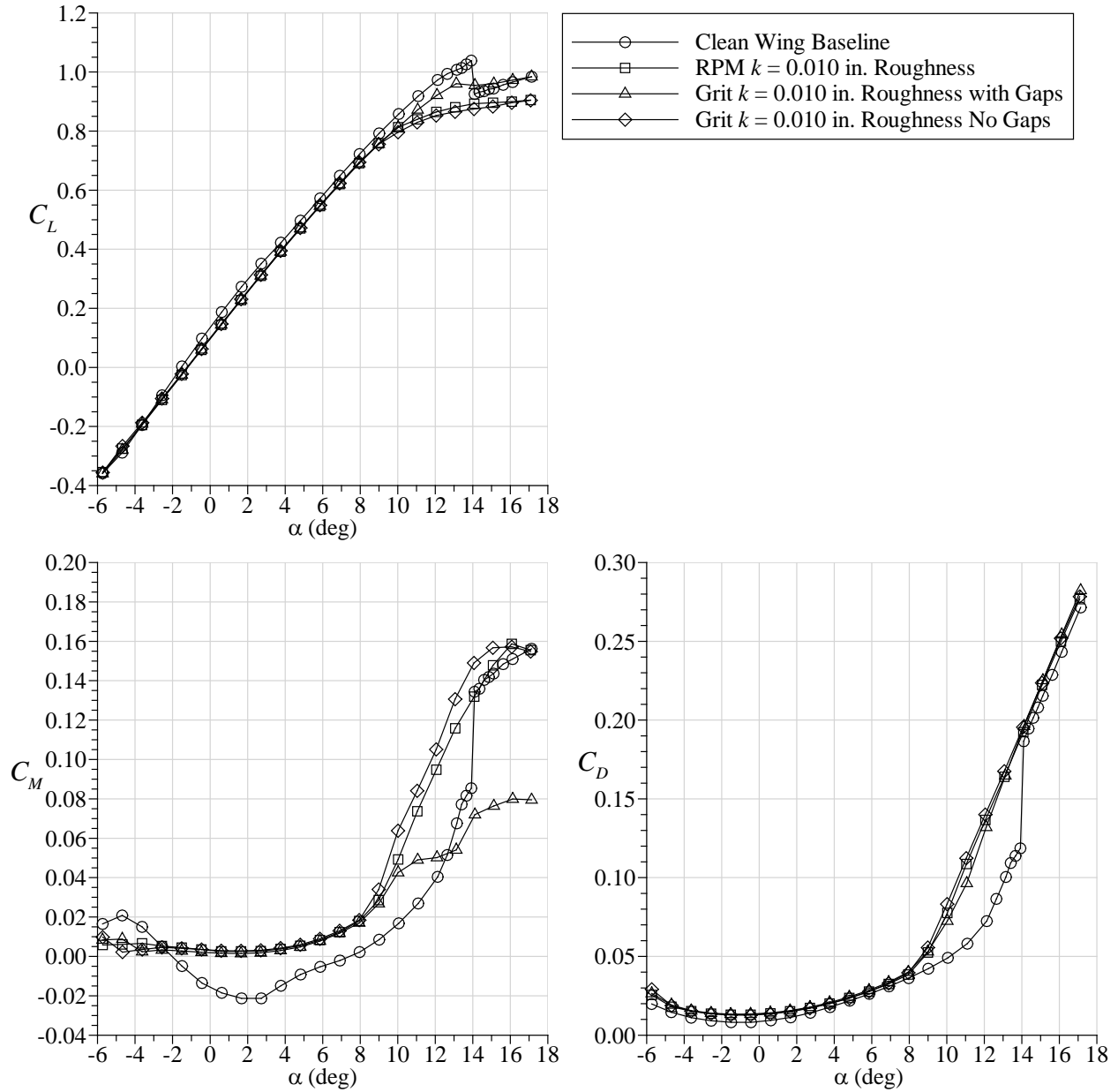

Figure 27. Effect of RPM- and grit-based artificial ice roughness on wing performance at $Re = 1.6 \times 10^6$ and $M = 0.18$

In addition to the artificial ice roughness, one large horn-type artificial ice configuration was also tested in this preliminary campaign. The geometry details were provided in section 2.3. The aerodynamic performance effect of this ice shape is shown in figure 28 along with the RPM $k = 0.02$-in. roughness for comparison. The horn-ice shape did have a significant impact on the wing aerodynamics. As was the case for the artificial ice roughness, it is difficult to unambiguously define the stalling angle of attack based on these data. There was a significant change in the slopes of C_M and C_D versus α beginning at approximately $\alpha = 6°$. Figure 29 shows a comparison of the surface pressure distributions near this angle of attack at pressure Row 5 ($y/b = 0.44$) near the model midspan location. There were only minor differences between the clean wing and wing with $k = 0.020$-in. RPM roughness configurations at this spanwise location. This is contrasted with the large effect of the horn-ice shape attached to the wing that caused a complete redistribution of suction pressure on the forward portion of this wing section. This resulted from the formation of the leading-edge vortex emanating from the artificial ice horn. Increasing the angle of attack up to 7.9° in figure 30 indicates what was likely an entire region of separated flow behind the horn-ice shape at this spanwise location. The plot also shows that the $k = 0.020$-in. RPM-based roughness had a significant effect on the wing pressures at this spanwise location and angle of attack.
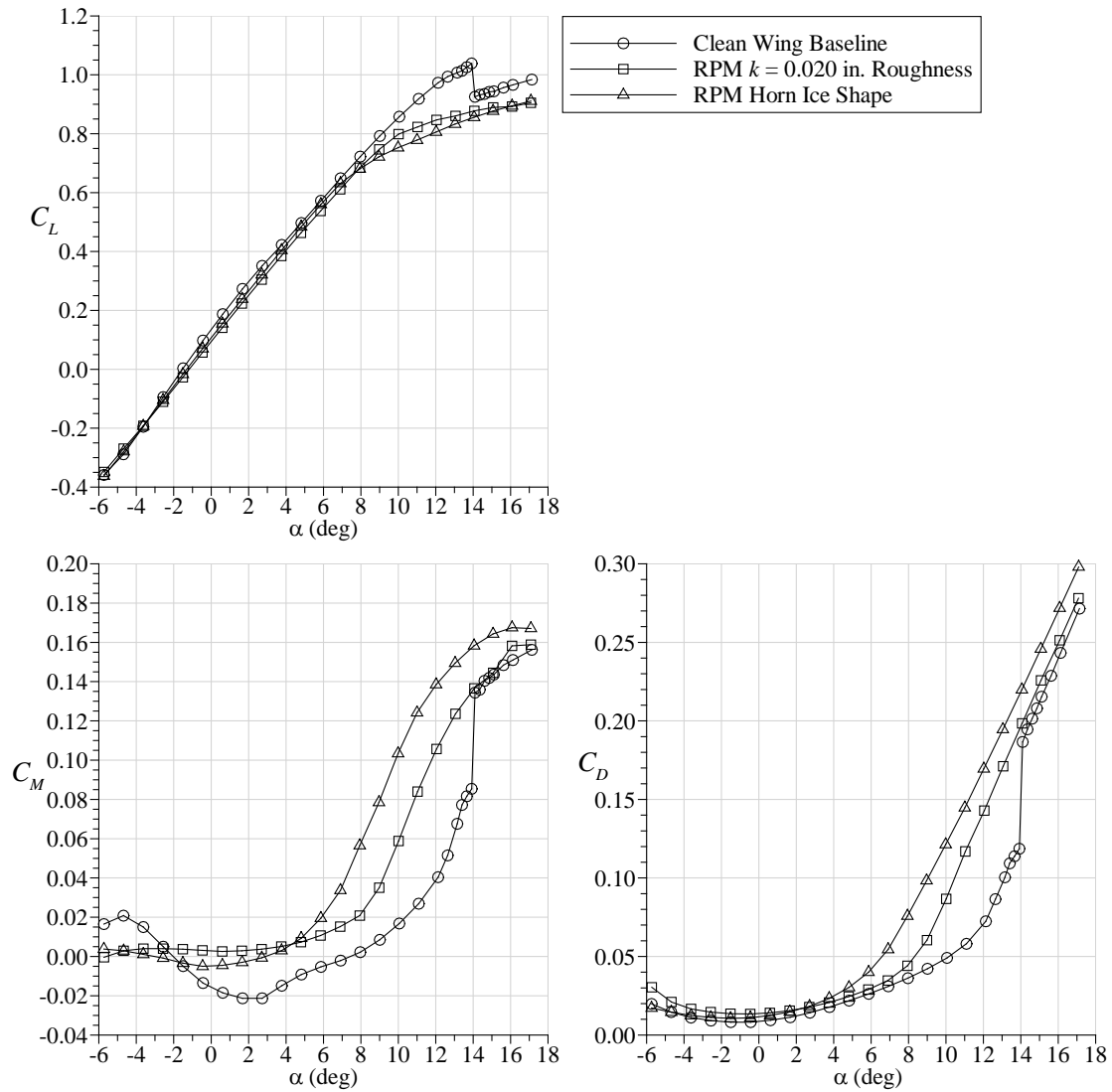
Figure 28. Effect of RPM-based artificial ice roughness and RPM-based artificial horn ice on wing performance at $Re = 1.6 \times 10^6$ and $M = 0.18$

Figure 29. Effect of RPM-based artificial ice roughness and RPM-based artificial horn ice on surface pressure distribution at $Re = 1.6 \times 10^6$ and $M = 0.18$, ROW 5, $y/b = 0.44$, $\alpha = 5.9°$
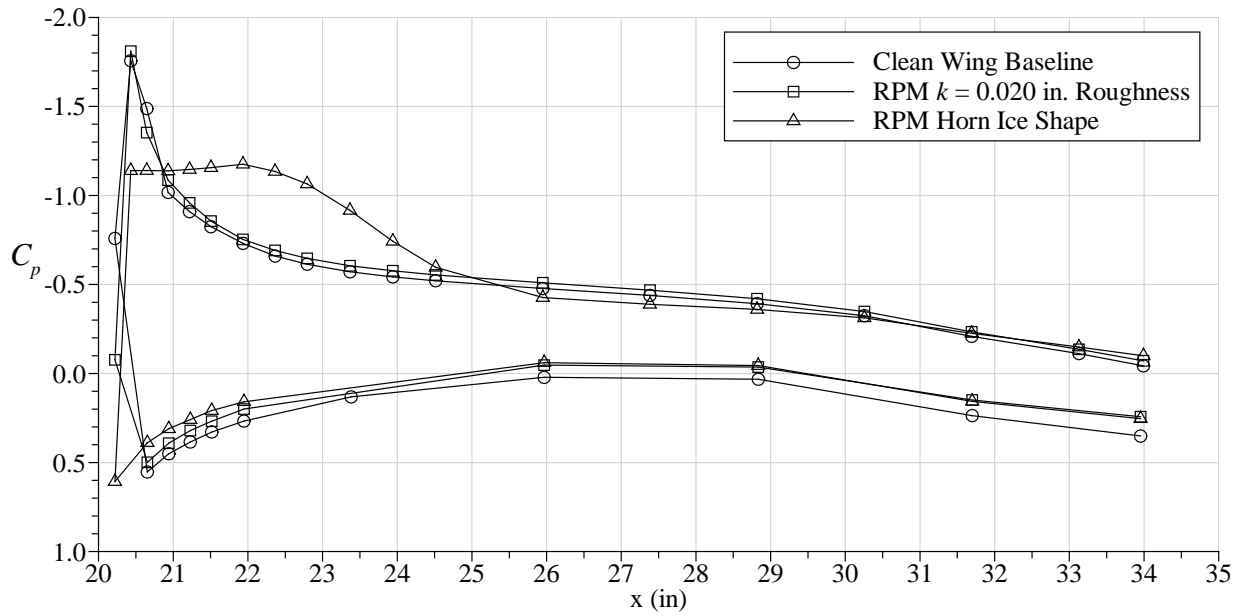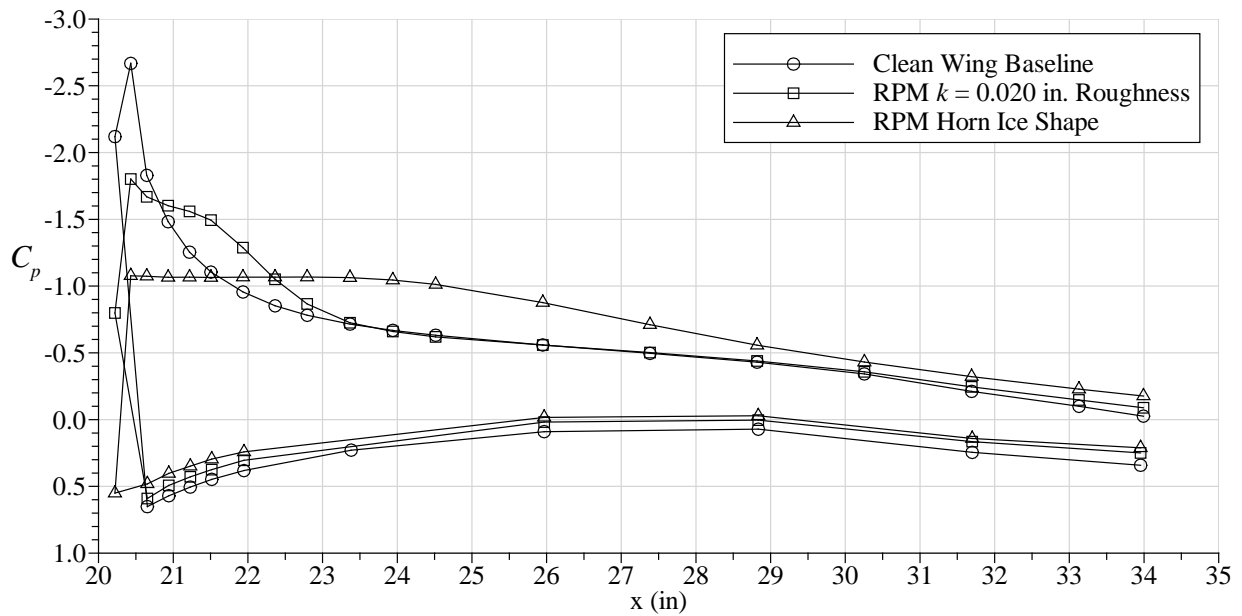

Figure 30. Effect of RPM-based artificial ice roughness and RPM-based artificial horn ice on surface pressure distribution at $Re = 1.6 \times 10^6$ and $M = 0.18$, ROW 5, $y/b = 0.44$, $\alpha = 7.9°$

This preliminary investigation into the effects of artificial ice roughness and horn ice on the swept-wing performance has yielded some valuable insights in iced-wing performance. For example, defining an unambiguous stalling angle could be challenging using only performance-based parameters. Further analysis of the wing surface pressure and flow visualization is needed to develop a better definition of the iced-wing stall. Plans for future test campaigns call for wake surveys that should provide significantly more details about the wing performance, such as the spanwise distributions of lift and drag. Practical results from this work include the significant effects of spanwise gaps or breaks in artificial roughness or ice shapes. This knowledge will help to improve the fidelity of artificial ice shapes developed for future test campaigns.

3.2.2 Reynolds and Mach Number Effects

The effects of Reynolds and Mach number variations on the iced-wing performance were found to be very small relative to the larger effects of the artificial roughness or ice shape on the clean-wing performance. The latter was quantified in section 3.2.1. The former is quantified here, specifically in figure 31 for the artificial horn-ice shape. It is fair to say that differences in Reynolds and Mach number had some effect on the pitching moment. The horn-ice simulation was intended to be an example of a larger (but realistic) ice shape for this wing. Based on the vast database of iced-airfoil aerodynamics, it was expected that the wing performance with the large horn ice would not exhibit any dependence on Reynolds and Mach number over the range tested in this investigation. The ice roughness simulations were intended to represent some of the smallest sizes of realistic ice roughness for this wing. Figure 32 shows the effect of Reynolds and Mach number on the wing performance with the RPM-based $k = 0.010$-in. roughness. In this case, there was more variation, particularly for the lowest Reynolds and Mach number and in the post-stall region (i.e., $\alpha > 8°$). As was noted in section 3.1.2, it is difficult, if not impossible, to ascertain meaningful conclusions regarding Reynolds and Mach number effects based on the small range of conditions available in this facility. Results from pressure-tunnel tests in the ONERA F1 facility will provide much better insight.
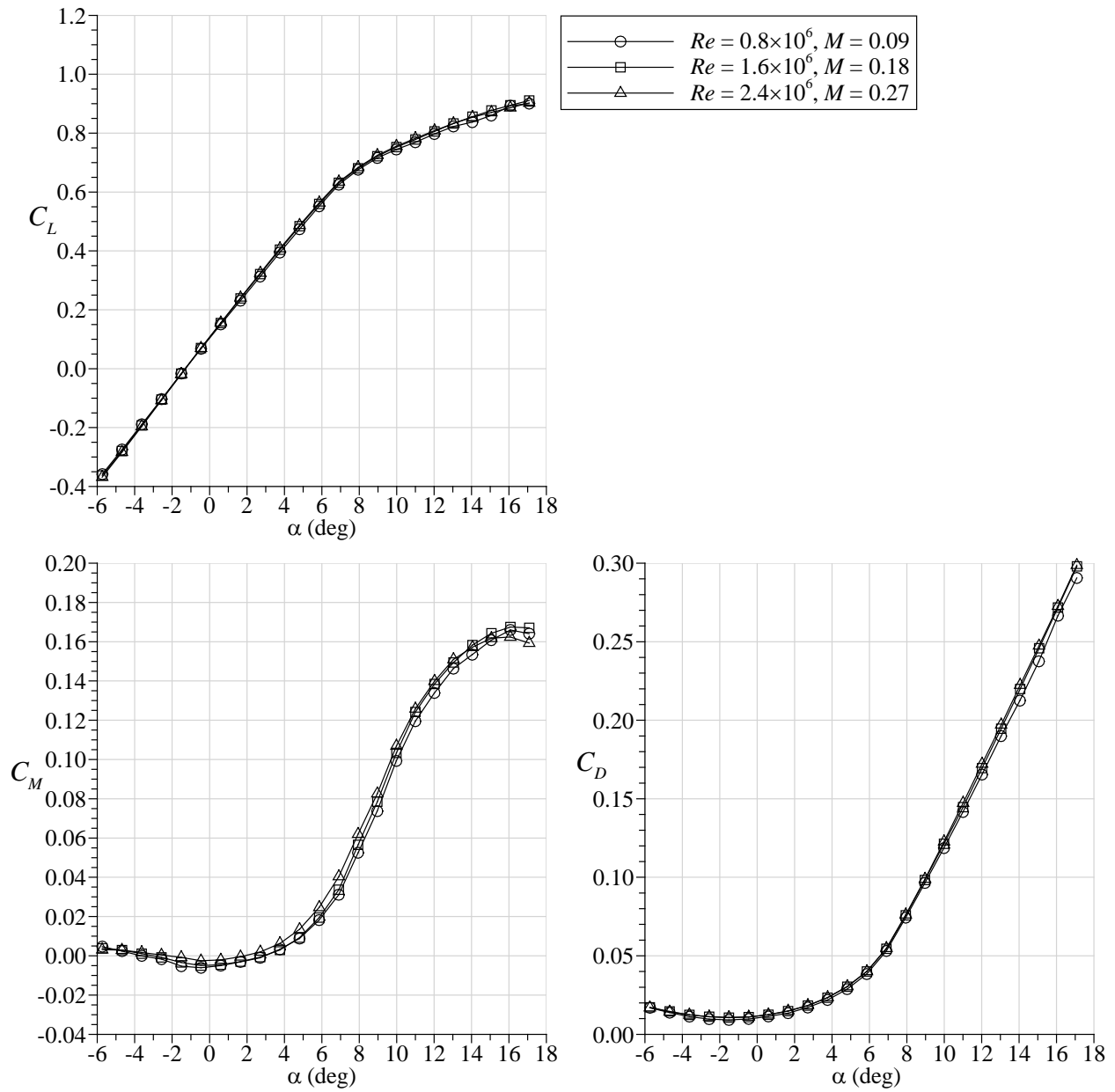
Figure 31. Effect of Reynolds and mach number on wing performance with RPM-based artificial horn-ice shape
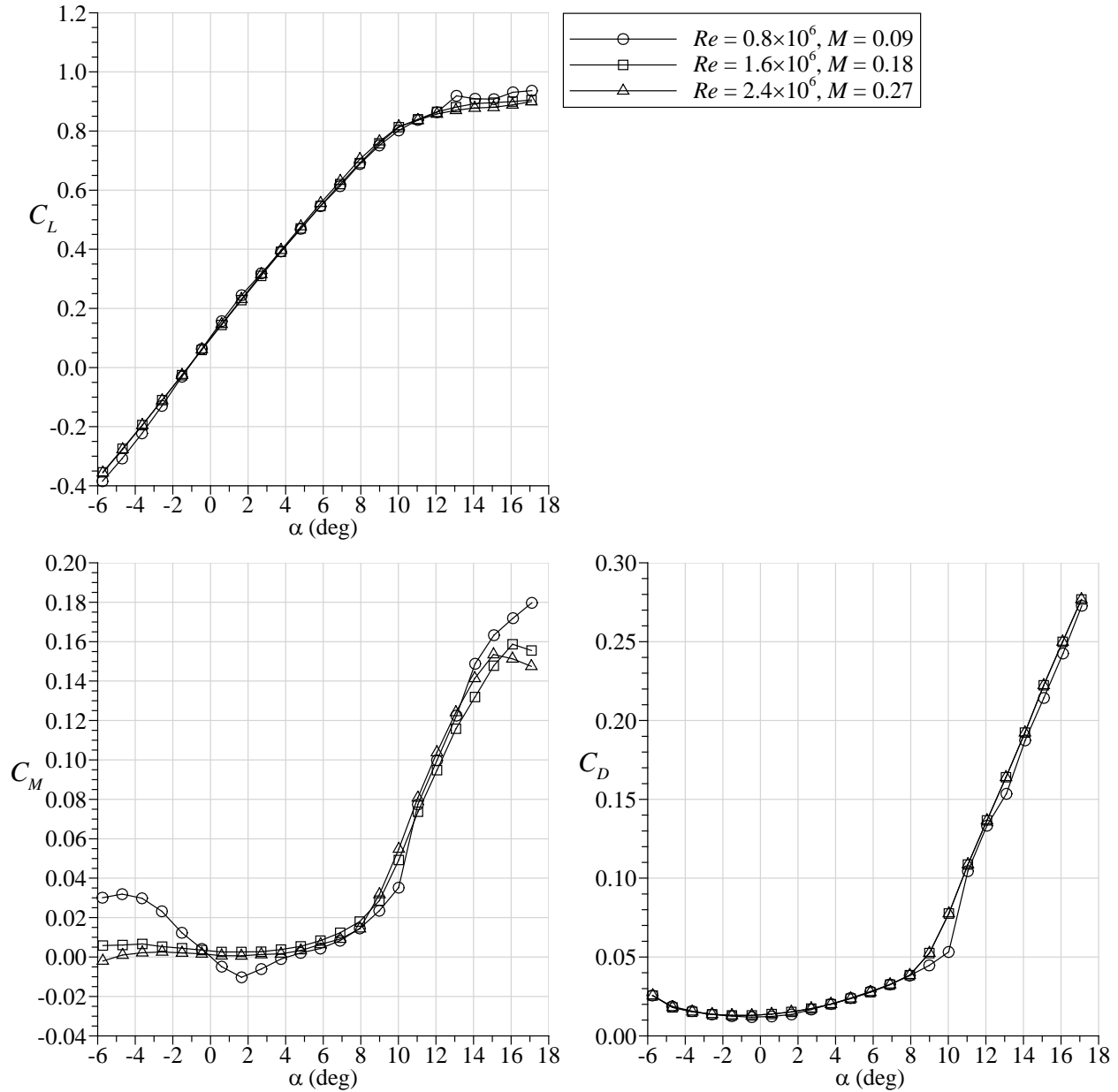
Figure 32. Effect of Reynolds and mach number on wing performance with RPM-based
$k = 0.010$-in. artificial ice roughness

3.2.3 Flow Visualization

Surface oil flow visualization was performed on the swept-wing model with RPM-based artificial ice roughness, grit roughness, and the RPM-based artificial horn ice at a Reynolds number of 1.6×10^6 and Mach number of 0.18. The flow visualization with the RPM-based artificial ice roughness is shown in figure 33 for the case $k = 0.010$ in. The previously shown performance data indicated that the stall process was especially gradual for this wing with surface roughness added. The flow visualization is shown before and after stall, at $\alpha = 9.0°$ and 13.1°, respectively. The flow was attached at $\alpha = 9.0°$ and appears similar to the clean case image shown in figure 23 for the

same angle of attack. In contrast, the flow visualization image at α = 13.1° shows that the leading-edge vortex was located farther inboard on the model relative to the clean configuration. Other disturbances to the flowfield are evident in figure 33 and are labeled. Toward the tip of the model, the seams between the RLE segments affected the flow pattern in the oil and even the discontinuity in the artificial roughness pattern because the pressure taps changed the flowfield. Several of the roughness elements were removed from the regular pattern around each of the pressure taps. The interface seam between RLE segments was a different style in the outboard portions of the model compared to the inboard, so that may explain why the effect of the seam is obvious only on a portion of the model. The reason that the roughness discontinuity only affects the flow outboard is not clear from the analysis of these images.
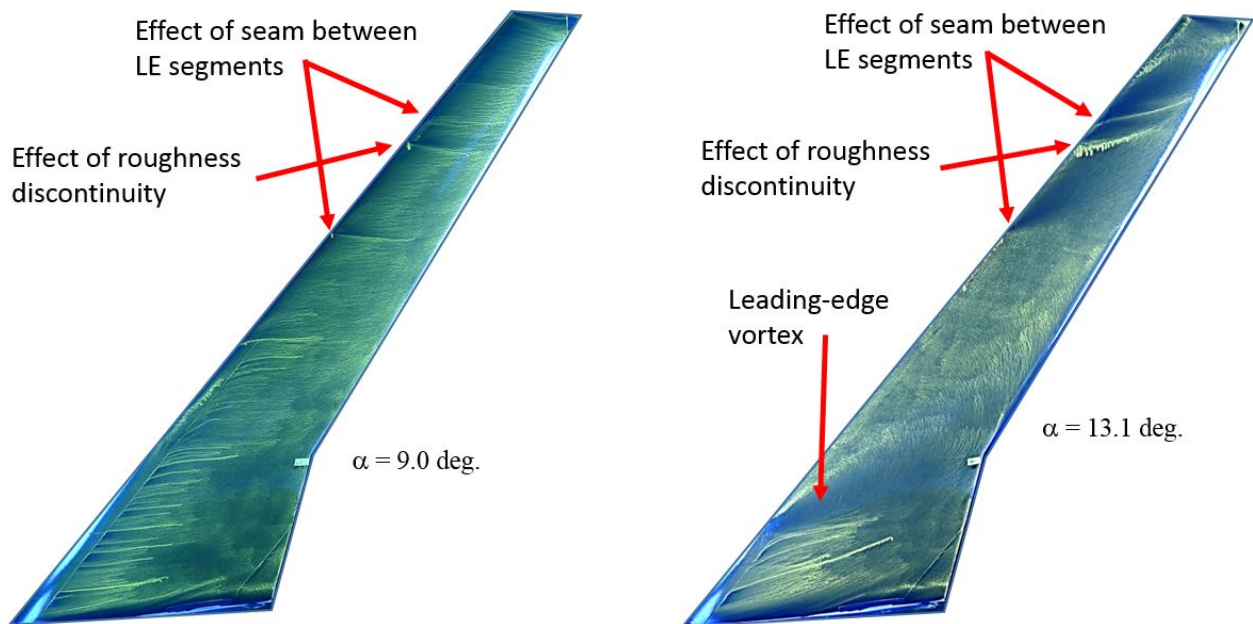

Figure 33. Surface oil flow visualization comparison for k = 0.010 in. RPM-based artificial ice roughness at Re = 1.6 × 10⁶ and M = 0.18

Oil flow images were also acquired with the grit-based roughness applied to the model (see figure 34). The grit roughness size was also k = 0.010 in. The same two angles of attack are shown comparing the grit-based roughness to the RPM-based roughness (α = 9.0° and 13.1°). The major features of the flowfield are consistent in figure 33 and 34. For α = 9.0°, the flow was attached. For α = 13.1°, the leading-edge vortex appeared to be in the same location as in figure 33. The cause of the other flow features in the α = 13.1° case is not obvious. The grit was applied to the clean aluminum leading edge so no seams existed along the leading edge, but gaps were left in the grit at the pressure tap row locations (see section 2.3). These gaps affected the performance of the wing (see section 3.2).
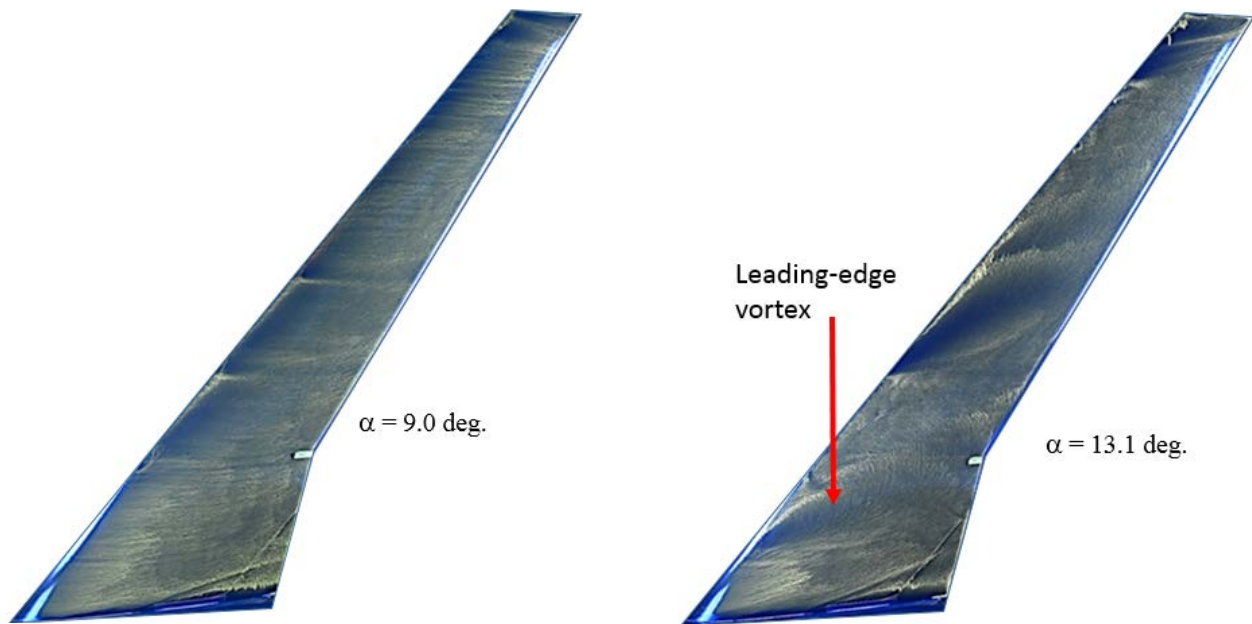
Figure 34. Surface oil flow visualization comparison for $k = 0.010$-in. grit-based artificial ice roughness at $Re = 1.6 \times 10^6$ and $M = 0.18$

Flow visualization was also performed with the RPM-based artificial horn-ice shape to determine its effect on the flowfield. In figure 35, the wing is shown before stall begins ($\alpha = 4.8°$) and as the stall progresses ($\alpha = 6.9°$ and $\alpha = 11.0°$). At $\alpha = 4.8°$, the flow separated from the tip of the horn ice but quickly reattached forming a spanwise leading-edge vortex that, while present, is difficult to see in the image. Once the separated flow reattached downstream of the ice shape, it remained attached across the chord of the model, as evident in the image. This attached flow across the majority of the wing is similar to the flow behavior at $\alpha = 9.0°$ for the clean wing and wing with roughness added cases. For the case at $\alpha = 6.9°$, the vortex that formed as the flow separated from the ice shape is evident across most of the span. The reattachment line of this vortex can be seen on close investigation of the image, and its position is highlighted with the red line in figure 35. At $\alpha = 11.0°$, the leading-edge vortex can still be seen, but the reattachment line can no longer be seen along the model because the flow was completely separated outboard of the vortex.
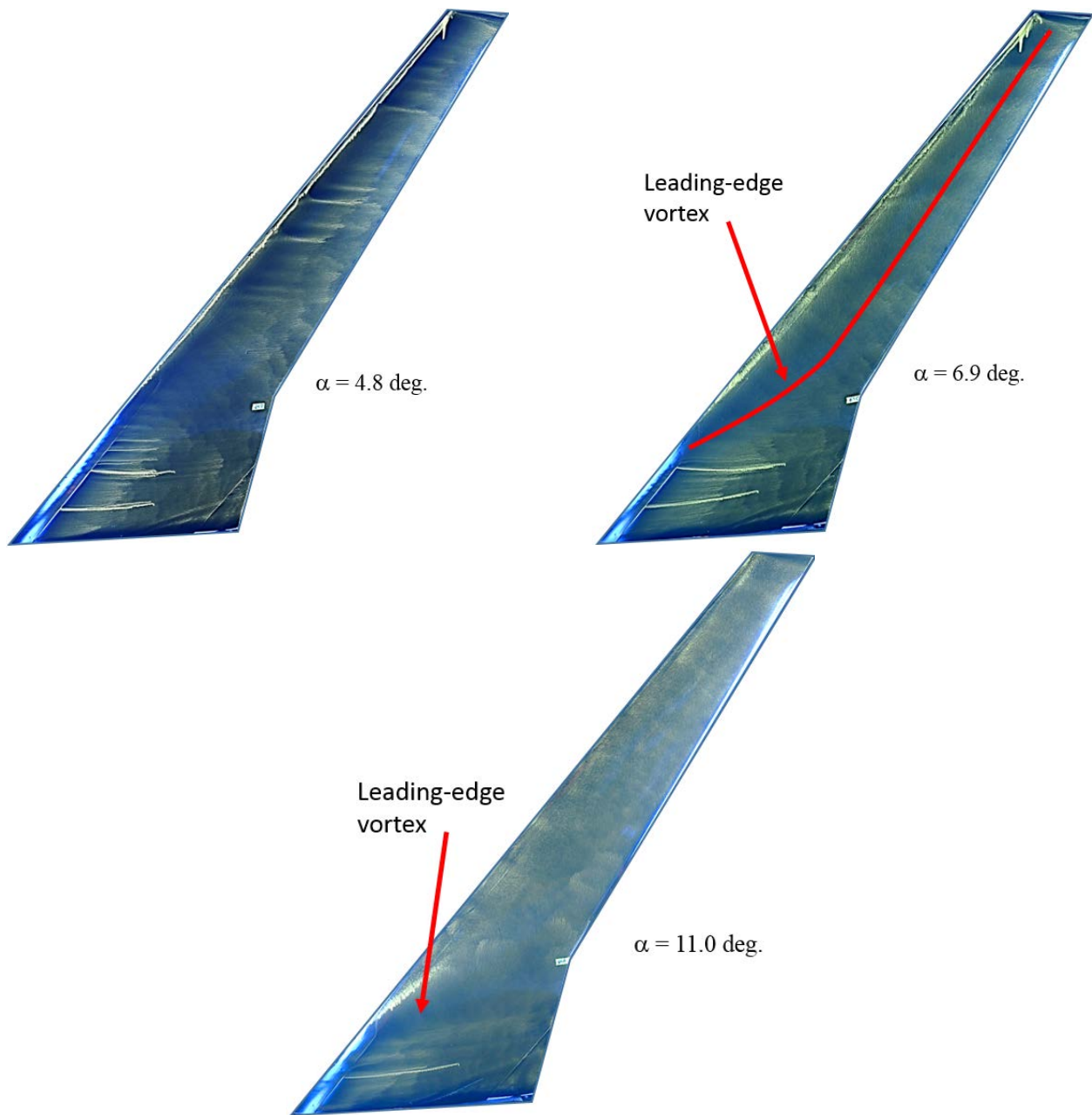
Figure 35. Surface oil flow visualization comparison for RPM-based artificial horn ice at
$Re = 1.6 \times 10^6$ **and** $M = 0.18$

Pressure coefficient data are shown in figure 36 for the same three angles of attack shown in figure 35 at three spanwise locations ($y/b = 0.28$, 0.60, and 0.81). At $\alpha = 4.8°$, the pressure distribution is consistent with separated flow directly downstream of the horn ice and then reattached flow downstream. The leading-edge vortex in the $\alpha = 6.9°$ case affects the pressure distribution similarly at each of the spanwise stations but does not drastically change the character compared to the lower angle of attack case. At the highest angle of attack ($\alpha = 11.0°$), the flow separation over most of the model is evident in the pressure distributions.

Figure 36. Comparison of RPM-based artificial horn ice surface pressure distribution at
$RE = 1.6 \times 10^6$ **AND** $M = 0.18$

4. SUMMARY, CONCLUSIONS, AND RECOMMENDATIONS

4.1 SUMMARY

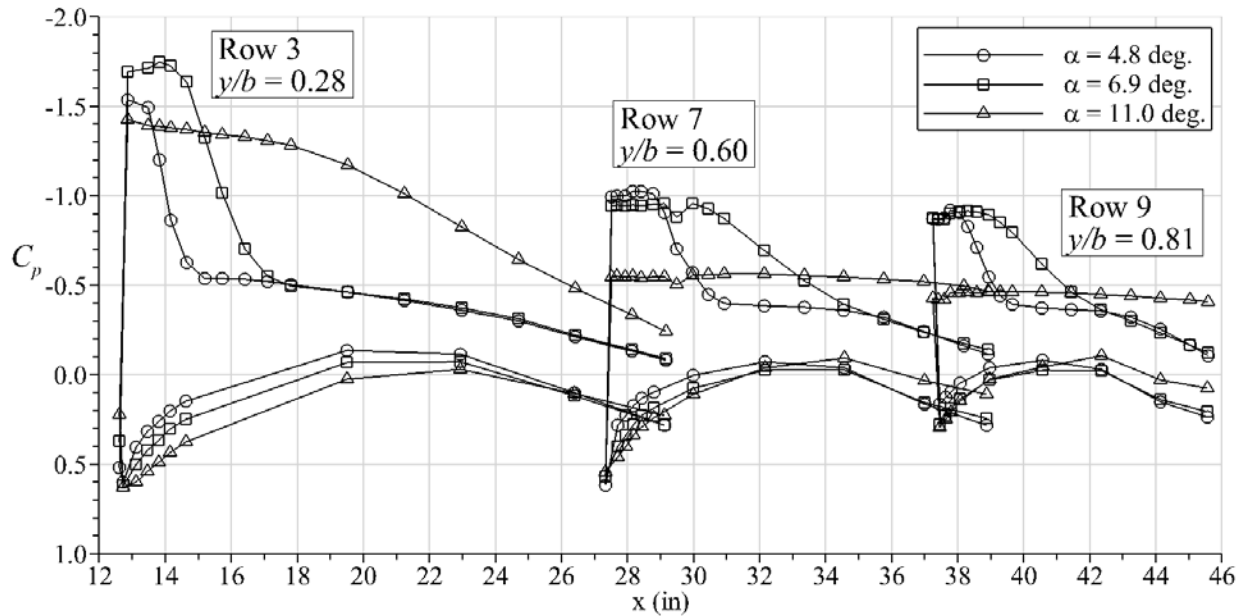A two-week wind-tunnel test campaign was performed in the Walter H. Beech wind-tunnel facility located at WSU using an 8.9% scale semispan model of the CRM65 wing. The objectives of the testing included: evaluating splitter plate configurations, evaluating the capability of RPM methods for capturing small-scale ice roughness features, evaluating the use of those RPM segments as a portion of the wind-tunnel model, and creating a preliminary assessment of the aerodynamic performance of this model at low Reynolds number. Aerodynamic performance testing was conducted in angle of attack sweeps at Reynolds numbers of 0.8×10^6, 1.6×10^6, and 2.4×10^6, corresponding to Mach numbers 0.09, 0.18, and 0.27, respectively. Force balance and surface pressure data were acquired. Surface oil flow visualization was also performed for a subset of the configurations after evaluating the aerodynamic data. The model had a span of 60 in. and a mean aerodynamic chord of 16.67 in. The design incorporated a RLE so that artificial ice shapes could be installed. Surface pressure taps were also installed throughout the model, and four different combinations of splitter plates and shrouds were designed to test different configurations. To evaluate the ability of RPM methods to capture small-scale ice roughness details, hemispheres of various sizes were added to segments of the RLE and fabricated. After evaluating these test pieces, hemispheres with radii of 0.01 in. and 0.02 in. were added across the span of the model with uniform spacing between hemispheres. The coverage extent was determined based on LEWICE3D simulations of a similar model in icing conditions. Grit roughness was also applied to the model with the same nominal sizes and 0.005 in. Those same LEWICE3D simulations also provided data for creating a full-span of horn ice shapes for the model that were also fabricated using RPM. Aerodynamic performance data and surface pressure data are presented for several comparisons. The splitter plate configurations are compared, the

47

Reynolds number and Mach number effects on the clean model are shown, and the effects of the various artificial ice shapes are illustrated. Surface oil flow images are also presented to illustrate the flowfield differences among the various leading-edge configurations.

4.2 CONCLUSIONS

After completing this preliminary test, many useful conclusions can be drawn that will assist the planning and execution of the future low and high Reynolds number campaigns. The splitter plate system with a circular cross-section splitter and streamlined shroud was selected to be the baseline configuration for these and future tests. The circular splitter stays at the same location relative to the leading edge of the wing regardless of angle of attack, and the streamlined shroud minimizes the blockage below the plate. An investigation was performed into the Reynolds number and Mach number effects on the clean-wing geometry. At low angles of attack, the wing's performance is similar at the three Reynolds numbers tested, but at higher angles, differences are evident in the aerodynamic performance data. Further differences are obvious in the surface pressure data based on the stalled regions of the model. However, more extensive analysis of Reynolds- and Mach-number effects will require the use of future studies from a pressurized wind tunnel in which Reynolds number and Mach number will be controlled independently. For the leading-edge configurations with roughness and horn ice, the Reynolds-number and Mach-number effects were small relative to the overall effect of the ice as compared to the clean-wing performance. Again, conclusions regarding the Reynolds- and Mach-number effects are limited by range afforded by the facility. Results from the iced wing configurations showed that defining an unambiguous stalling angle was difficult using only performance-based parameters. Further analysis of the wing surface pressure and flow visualization is required to provide a better understanding of the iced-wing stall. Performance differences between the various roughness sizes and applications types were small, especially at low angles of attack. Perhaps more importantly for this preliminary study, it was found that the method of applying the grit roughness had a relatively large impact on performance. In some cases, the grit covered the entire span without gaps, and in other cases, gaps were left at the pressure tap rows to collect those data. This result and the small performance differences observed between the rapid prototype manufacturing (RPM) clean leading edge and the machined, aluminum leading-edge cases indicate that the model is particularly sensitive to spanwise changes in the geometry. The surface oil flow images confirm that the variations along the leading edge affect the flowfield on the wing, though they do not help to quantify the effects.

4.3 RECOMMENDATIONS

This preliminary low Reynolds number wind-tunnel campaign provided useful lessons both scientifically and practically that will help to ensure successful future low and high Reynolds number tests. The splitter plate system design, including a circular splitter and streamlined shroud, will be used in all future tests. The leading-edge segments should be designed carefully to minimize unintentional spanwise variations by reducing the number of RPM segments. Therefore, future tests with this 8.9% scale model will use only two RPM leading-edge segments. Furthermore, the RPM leading-edge segments must be carefully designed to fit over the model easily to minimize the time required to complete ice-shape configuration changes. Because of the challenge of precisely defining the stall angle of the iced wing, a general stall criteria should be developed for the analysis of the data acquired in future campaigns. A wake survey diagnostic should be used in future tests because it will provide significantly more details about the wing

performance, such as the spanwise distributions of lift and drag. These measurements are planned for future low Reynolds number tests. The pressurized wind tunnel with separate control over Reynolds number and Mach number will provide a significantly more complete understanding of those effects compared to the data presented in this preliminary report. Attention should also be directed to determining the most appropriate wind-tunnel-wall correction scheme for these experiments. The upcoming wind-tunnel campaigns with realistic ice shapes created from icing wind-tunnel tests will provide a unique database of aerodynamic information that can be used to evaluate the icing performance of a modern, swept-wing configuration.

5. REFERENCES

1. AIAA. (2013). *Swept-Wing Ice Accretion Characterization and Aerodynamics* (AIAA Paper 2013-2824). Broeren, A. P., Potapczuk, M. G., Riley, J.T., Villiedieu, P., Moens, F., Bragg, M. B. (also published as NASA TM—2013-216555).

2. FAA Report. (2013). *Aerodynamic Classification of Swept-Wing Ice Accretion* (DOT/FAA/TC-13/21). (also published as NASA TM 2013-216381).

3. AIAA. (2013). *Aerodynamic Classification of Swept-Wing Ice Accretion* (AIAA Paper 2013-2825) Broeren, A. P., Diebold, J. M., and Bragg, M. B.

4. AIAA. (2012). *Aerodynamics of a Swept-Wing with Ice Accretion at Low Reynolds Number* (AIAA Paper 2012-2795) Diebold, J. M., Monastero, M. C., and Bragg, M. B.

5. Diebold, J.M. (2012). *Aerodynamics of a Swept Wing with Leading-Edge Ice at Low-Reynolds Number* (M.S. Thesis). Department of Aerospace Engineering, University of Illinois, Urbana, IL.

6. AIAA. (2013). *Study of a Swept-Wing with Leading-Edge Ice Using a Wake Survey Technique* (AIAA Paper 2013-0245). Diebold, J.M., and Bragg, M.B.

7. AIAA. (2012). *Development of 3-D Ice Accretion Measurement Method* (AIAA Paper 2012-2938). Lee, S., Broeren, A. P., Addy, H. E., Jr., Sills, R., and Pifer, E. M. (also published as NASA TM—2012-217702).

8. Monastero, M.C. (2013). *Validation of 3-D Ice Accretion Documentation and Replication Method Including Pressure-Sensitive Paint* (M.S. Thesis). Department of Aerospace Engineering, University of Illinois, Urbana, IL.

9. AIAA. (2014). *Implementation and Validation of 3-D Ice Accretion Measurement Methodology* (AIAA Paper 2014-2613). Lee, S., Broeren, A. P., Kreeger, R. E., Potapczuk, M. G., and Utt, L.

10. AIAA. (2014). *Validation of 3-D Ice Accretion Measurement Methodology for Experimental Aerodynamic Simulation* (AIAA Paper 2014-2614). Broeren, A.P., Lee, S. L., Addy, H. E., Jr., and Monastero, M. C.

11.   AIAA. (2014). *Validation of 3-D Ice Accretion Measurement Methodology Using Pressure-Sensitive Paint* (AIAA Paper 2014-2615). Monastero, M. C., and Bragg, M. B.

12.   Mortonson, A.J. (2011). *Use of Hybrid Airfoil Design in Icing Wind Tunnel Tests of Large Scale Swept Wings* (M.S. Thesis). Department of Aerospace Engineering, University of Illinois, Urbana, IL.

13.   AIAA. (2013). *A Hybrid Airfoil Design Method for Icing Wind Tunnel Tests* (AIAA Paper 2013-2826). Fujiwara, G. E. C., Woodard, B. S., Wiberg, B. D., Mortonson, A. J., Bragg, M. B.

14.   Wiberg, B. D. (2013). *Large-Scale, Swept-Wing Ice Accretion Modeling in the NASA Glenn Icing Research Tunnel Using LEWICE3D* (M.S. Thesis). Department of Aerospace Engineering, University of Illinois, Urbana, IL.

15.   AIAA. (2014). *3D Swept Hybrid Wing Design Methods for Icing Wind Tunnel Tests* (AIAA Paper 2104-2616). Fujiwara, G. E. C., Wiberg, B. D., Woodard, B. S., and Bragg, M. B.

16.   AIAA. (2014). *Large-Scale, Swept-Wing Icing Simulations in the NASA Glenn Icing Research Tunnel Using LEWICE3D* (AIAA Paper 2014-2617). Wiberg, B. D., Fujiwara, G. E. C., Woodard, B. S., and Bragg, M. B.

17.   Fujiwara, G.E.C. (2014). *Design of 3D Swept Wing Hybrid Models for Icing Wind Tunnel Tests* (M.S. Thesis). Department of Aerospace Engineering, University of Illinois, Urbana, IL.

18.   ONERA. (2014). *Rapport D'advancement du Projet SUNSET 2 en 2013* (ONERA Rapport Final N° RF 1/21372 DMEA/DAAP/DSNA). Moens, F., Costes, M., Terracol, M., Radenac, E., Trontin, P., and Villedieu, P.

19.   AIAA. (2014). *Computational Aerodynamic Analysis of Three-Dimensional Ice Shapes on a NACA 23012 Airfoil* (AIAA Paper 2104-2202). Jun, G., Oliden, D., Potapczuk, M. G., and Tsao, J-C.

20.   ONERA. (2015). *Rapport D'advancement du Projet SUNSET 2 en 2014* (ONERA Rapport Final N° RF 1/22549 DMEA/DAAP/DSNA). Costes, M., Terracol, M., Michel, B., Radenac, E., Gaible, H., and Bezard, H.

21.   SAE. (2015). *Detached Eddy Simulation on a Swept Hybrid Model in the IRT* (SAE Paper 2015-01-2122). Butler, C., and Loth, E.

22.   NASA. (1987). *A Study of High-Lift Airfoils at High Reynolds Numbers in the Langley Low-Turbulence Pressure Tunnel* (NASA TM-89125). Morgan, H. L., Ferris, J. C., and McGhee, R. J.

23. AIAA. (2000). *A Wind Tunnel Study of Icing Effects on a Natural Laminar Flow Airfoil* (AIAA Paper 2000-0095). Addy, H. E., Jr., and Chung, J. J. (also published as NASA/TM—2000-209775).

24. FAA Report. (2000). *Ice Accretions and Icing Effects for Modern Airfoils* (DOT/FAA AR-99/89). (also published as NASA/TP-2000-210031).

25. AIAA. (2003). *A Wind Tunnel Study of Icing Effects on a Business Jet Airfoil* (AIAA Paper 2003-0727). Addy, H. E., Jr., Broeren, A. P., Zoeckler, J. G., and Lee, S. (also published as NASA/TM—2003-212124).

26. Bragg, M. B., Broeren, A. P., and Blumenthal, L. A. (2005). Iced-Airfoil Aerodynamics, *Progress in Aerospace Sciences*, *41*(5), 323-418.

27. Broeren, A. P., Bragg, M. B., and Addy, H. E., Jr. (2004). Effect of Intercycle Ice Accretions on Aerodynamic Performance, *Journal of Aircraft, 41*(1), 165-174.

28. Broeren, A. P., Bragg, M. B., Addy, H. E., Jr., Lee, S., Moens, F., and Guffond, D. (2010). Effect of High-Fidelity Ice Accretion Simulations on the Performance of a Full-Scale Airfoil Model*, Journal of Aircraft, 47*(1), 240-254. (also published as NASA/TM-2010-216344).

29. AIAA. (2008). *Development of a Common Research Model for Applied CFD Validation Studies* (AIAA Paper 2008-6919). Vassberg, J. C., DeHann, M. A., Rivers, S. M., and Wahls, R. A.

30. AIAA. (2015). *Experimental Study of Splitter Plates for Use with Semispan Wing Models* (AIAA Paper 2015-1227). Diebold, J. M., Woodard, B. S., Monastero, M. C., and Bragg, M. B.

31. Diebold, J. M., Woodard, B. S., Camello, S., and Bragg, M. B. (2015). *Effect of Ice Accretion on Full-Scale, Swept-Wing Aerodynamic Performance and Control Effects*. Manuscript submitted for publication.

32. NASA. (2011). *Aerodynamic Simulation of Ice Accretion on Airfoils* (NASA TP—2011-216929). Broeren, A. P., Addy, H. E., Jr., Bragg, M. B., Busch, G. T., Guffond, D., and Montreuil, E.

33. Pope, A., Rae, W. H., and Barlow, J.B. (1999). *Low-Speed Wind Tunnel Testing* (3rd ed.). Hoboken, NJ: John Wiley & Sons, Inc.

34. "Data Reduction System: Boundary Corrections," Walter H. Beech Memorial Wind Tunnel Engineering Process Description, 2014.

35. Coleman, H. W. and W. G. Steel, J. (1989). *Experimentation and Uncertainty Analysis for Engineers*. Hoboken, NJ: John Wiley & Sons, Inc.

36.   Realize Inc., (2016). Retrieved from http://www.realizeinc.com/aboutus/ .